

# Atomistic simulations of the *Escherichia coli* ribosome provide selection criteria for translationally active substrates

Received: 1 September 2022

Zoe L. Watson  <sup>1,2,3</sup>, Isaac J. Knudson <sup>1,2</sup>, Fred R. Ward  <sup>2,4</sup>, Scott J. Miller  <sup>2,5</sup> , Jamie H. D. Cate  <sup>1,2,4,6</sup> , Alanna Schepartz  <sup>1,2,3,4,6,7</sup>  & Ara M. Abramyan  <sup>8</sup> 

Accepted: 28 April 2023

Published online: 12 June 2023

 Check for updates

As genetic code expansion advances beyond L- $\alpha$ -amino acids to backbone modifications and new polymerization chemistries, delineating what substrates the ribosome can accommodate remains a challenge. The *Escherichia coli* ribosome tolerates non-L- $\alpha$ -amino acids in vitro, but few structural insights that explain how are available, and the boundary conditions for efficient bond formation are so far unknown. Here we determine a high-resolution cryogenic electron microscopy structure of the *E. coli* ribosome containing  $\alpha$ -amino acid monomers and use metadynamics simulations to define energy surface minima and understand incorporation efficiencies. Reactive monomers across diverse structural classes favour a conformational space where the aminoacyl-tRNA nucleophile is  $<4$  Å from the peptidyl-tRNA carbonyl with a Bürgi–Dunitz angle of 76–115°. Monomers with free energy minima that fall outside this conformational space do not react efficiently. This insight should accelerate the in vivo and in vitro ribosomal synthesis of sequence-defined, non-peptide heterooligomers.

The ribosome is a biological machine that faithfully converts information embodied in one polymer into a different polymer with minimal information loss, synonymous codons notwithstanding. Although the process of mRNA translation enables vast and sophisticated functions throughout biology, the protein chemical space in extant organisms is limited to about 20 natural  $\alpha$ -amino acids and, before post-translational modifications, an invariant peptide backbone. Twenty-plus years of genetic code expansion has broadened protein chemical space to include greater than 200 non-natural  $\alpha$ -amino acids<sup>1</sup>. However, with two exceptions<sup>2,3</sup>, protein chemical space in vivo is limited to  $\alpha$ -amino and (a few)  $\alpha$ -hydroxy acids and an otherwise invariant peptide backbone<sup>4–7</sup>.

By contrast, access to alternative backbones is more widespread in vitro, where the concentration of chemically produced

acyl-tRNA can be 50 times higher than possible in vivo. Under such conditions, *E. coli* ribosomes support bond-forming reactions between monomers whose backbones deviate considerably from native  $\alpha$ -amino acids<sup>8–15</sup>. The structural and electronic diversity of these monomers underscores the importance of proximity in promoting bond-forming reactions within the *E. coli* peptidyl transferase centre (PTC; Fig. 1a)<sup>16</sup>. Yet the yields of peptides containing these unusual monomers vary widely, and the products are often detected only by use of autoradiography or mass spectrometry. Given the potential of the ribosome for novel bond-forming chemistry, one must ask: what structural features define reactive monomers? Here we describe the implementation of a structurally informed computational workflow to identify promising monomers with speed, high accuracy and low cost.

<sup>1</sup>Department of Chemistry, University of California, Berkeley, CA, USA. <sup>2</sup>Center for Genetically Encoded Materials, University of California, Berkeley, CA, USA. <sup>3</sup>California Institute for Quantitative Biosciences (QB3), University of California, Berkeley, CA, USA. <sup>4</sup>Department of Molecular and Cellular Biology, University of California, Berkeley, CA, USA. <sup>5</sup>Department of Chemistry, Yale University, New Haven, CT, USA. <sup>6</sup>Molecular Biophysics and Integrated Bioimaging Division, Lawrence Berkeley National Laboratory, Berkeley, CA, USA. <sup>7</sup>Chan Zuckerberg Biohub, San Francisco, CA, USA. <sup>8</sup>Schrödinger, Inc., San Diego, CA, USA.  e-mail: [scott.miller@yale.edu](mailto:scott.miller@yale.edu); [j-h-doudna-cate@berkeley.edu](mailto:j-h-doudna-cate@berkeley.edu); [schepartz@berkeley.edu](mailto:schepartz@berkeley.edu); [ara.abramyan@schrödinger.com](mailto:ara.abramyan@schrödinger.com)

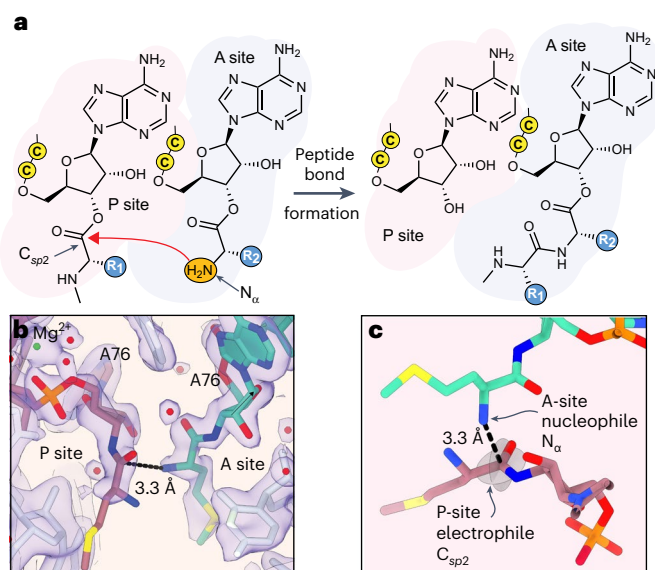


**Fig. 1 | Substrate positioning in the PTC.** **a**, Schematic depicting peptide bond formation in the ribosome active site known as the PTC. The PTC promotes peptide bond formation by positioning the nucleophilic  $\alpha$ -amino group ( $N_{\alpha}$ ) of one substrate, the A-site aminoacyl-tRNA, near the electrophilic  $sp^2$ -hybridized carbonyl carbon ( $C_{sp2}$ ) of the second substrate, the P-site peptidyl-tRNA. Attack by  $N_{\alpha}$  generates a tetrahedral intermediate that subsequently breaks down to product: a peptidyl-tRNA carrying an additional C-terminal amino acid. Cytidine residues of the tRNAs' 3'-CCA ends are represented by the letter 'C' in a yellow circle. **b**, Cryo-EM density (indigo surface) and our model for Met residues in the PTC. The distance between the A-site (green) nucleophilic amine and the P-site (rose) carbonyl carbon (3.3 Å) is indicated with a black dotted line. The 23S rRNA is shown in white. The  $Mg^{2+}$  ion that coordinates the C75–A76 internucleotide phosphate is shown in green. Note that an amide linkage is shown between the A76 and Met residues of each tRNA to reflect the experimental substrates used for structure determination; however, for simulation, this was replaced with the ester linkage that would be present during an elongation reaction. The map here was post-processed with a B-factor of  $-13 \text{ \AA}^2$  and supersampled for smoothness. **c**, Alternative view of the A-site and P-site Met residues highlighting the planes of the carbonyl that define the Bürgi–Dunitz ( $\alpha_{BD}$ ) and Flippin–Lodge ( $\alpha_{FL}$ ) angles and the geometry of nucleophilic attack.

We faced three challenges in implementing such a computational schema. First, the size of the ribosome—1.5 MDa in the *E. coli* large ribosomal subunit, not including substrates and solvation—pushes computational methods to their limit<sup>17,18</sup>. As a result, several coarse-grained<sup>19</sup>, normal mode analysis<sup>20</sup> and elastic network<sup>21</sup> models combined with simplified ribosome representations have been developed. While these simplifications reduce computational cost and adequately describe large-scale motions, they fail to capture atomistic details. By contrast, density functional theory (DFT) can provide atomistic and electronic details but cannot yet evaluate *de novo* how new monomers engage the PTC in the absence of experimental constraints on orientations in the active site<sup>22</sup>.

The second challenge is that the ribosome is a ribozyme<sup>23</sup>. Most structure-based modelling tools in wide use were developed to study protein enzymes. RNA contains more degrees of freedom than protein, and the polyanionic composition demands accurate, long-range electrostatic and solvation models that include explicit metal ions and water, especially within the PTC<sup>24</sup>. Conformational dynamics alone remains an enormous challenge for computational analyses, with increasing challenges as the complexity of the system increases<sup>25</sup>. While others have used three-dimensional (3D) puzzles for RNA structural predictions<sup>26</sup>, physics-based methods such as molecular dynamics (MD) simulations provide a more accurate description of the atomistic dynamics of biological systems<sup>27–29</sup>.

The final challenge is the choice of an appropriate high-resolution reference state. The highest-resolution structure of the ribosome available at the time of this work was Protein Data Bank (PDB) 7K00 (ref. 30). This cryogenic electron microscopy (cryo-EM) structure includes the 70S *E. coli* ribosome in complex with tRNA and mRNA substrates at 2 Å global resolution. Although local resolution surpassed this value in regions of the large subunit, the PTC itself was less well resolved, and the monomers could not be modelled (Extended Data Fig. 1a). PDB 6XZ7 (ref. 31) is also high resolution (2.1 Å) but contains product-like tRNAs (Extended Data Fig. 1b); PDB 1VY4 (ref. 24) contains reactant-like tRNAs, but the lower resolution (2.6 Å) as well as local map quality of amino acids in the PTC obscures details of monomer placement. We concluded that neither PDB 7K00, nor 6XZ7, nor 1VY4 represented an ideal starting point for simulations to evaluate the conformational landscape of non-L- $\alpha$ -amino acid monomers in the *E. coli* PTC; a structure with well-resolved monomers was required.

Here we present a cryo-EM structure of the *E. coli* ribosome that reaches 2.1 Å global resolution in the large subunit and visualizes natural methionine monomers and full-length tRNAs at improved resolution. Using a model derived from this structure, we executed metadynamics simulations to define the conformational free energy surfaces (FESs) of multiple structurally and stereochemically diverse non- $\alpha$ -amino acid monomers within the PTC. Minima in these FESs clearly differentiate reactive and non-reactive monomers: reactive monomers across all structural classes populate a conformational space characterized by an A-site nucleophile to P-site carbonyl distance ( $N_{\alpha}$ – $C_{sp2}$  distance) of  $<4 \text{ \AA}$  and a Bürgi–Dunitz<sup>32</sup> angle ( $\alpha_{BD}$ ) of 76–115°. Monomers whose free energy minima lie outside a region in which the  $N_{\alpha}$ – $C_{sp2}$  distance is less than 4 Å, even with an acceptable Bürgi–Dunitz angle, do not react efficiently. Metadynamics provided both high accuracy and full conformational sampling of monomers, as well as of the ribosome catalytic centre in the explicit solvent and ion environment. Metadynamics is fast, accurate and relatively cost-efficient. More importantly, it addresses multiple challenges impeding the ribosome-promoted biosynthesis of diverse heterooligomers. For applications *in vivo*, metadynamics can prioritize monomers for which orthogonal aminoacyl-tRNA synthetase variants are needed. For applications *in vitro*, it can identify monomers that are more likely to react within the PTC of wild-type ribosomes. In all cases, it can identify those monomers for which engineered ribosomes are needed. The work reported here should accelerate the *in vivo* ribosomal synthesis of much sought but not yet achieved sequence-defined, non-peptide heterooligomers and improve the diversity of the *in vitro* mRNA display campaigns used in drug discovery.

## Results and discussion

### An improved *E. coli* PTC structure informs reactivity

We first established an improved PTC model that retained the high resolution of PDB 7K00 (ref. 30) and 6XZ7 (ref. 31) but included better-resolved  $\alpha$ -amino acid monomers in the A and P sites (Fig. 1b). We reasoned that the low monomer density seen in 7K00 was due at least in part to aminoacyl-tRNA hydrolysis during grid preparation. To eliminate hydrolysis, we acylated 3'-amino tRNA<sup>Met</sup> with Met and *E. coli* methionyl-tRNA synthetase (MetRS)<sup>33</sup>. With this hydrolysis-resistant substrate, we obtained a 2.1-Å-resolution cryo-EM structure of the *E. coli* 50S subunit from 70S complexes, which contains well-resolved Met-NH-tRNA<sup>Met</sup> in both the A and P sites (Extended Data Fig. 2). During data processing, a classification approach more involved than our approach for PDB 7K00 (ref. 30) was used to determine a balance between maximal particle inclusion for higher global resolution and more discriminating exclusion of particles without well-resolved tRNA CCA ends (Methods and Supplementary Fig. 1).

Local features of the PTC in the current map (Fig. 1b) are substantially improved from PDB 7K00 despite the lower 2.1 Å global resolution of the large subunit. This resolution was sufficient to

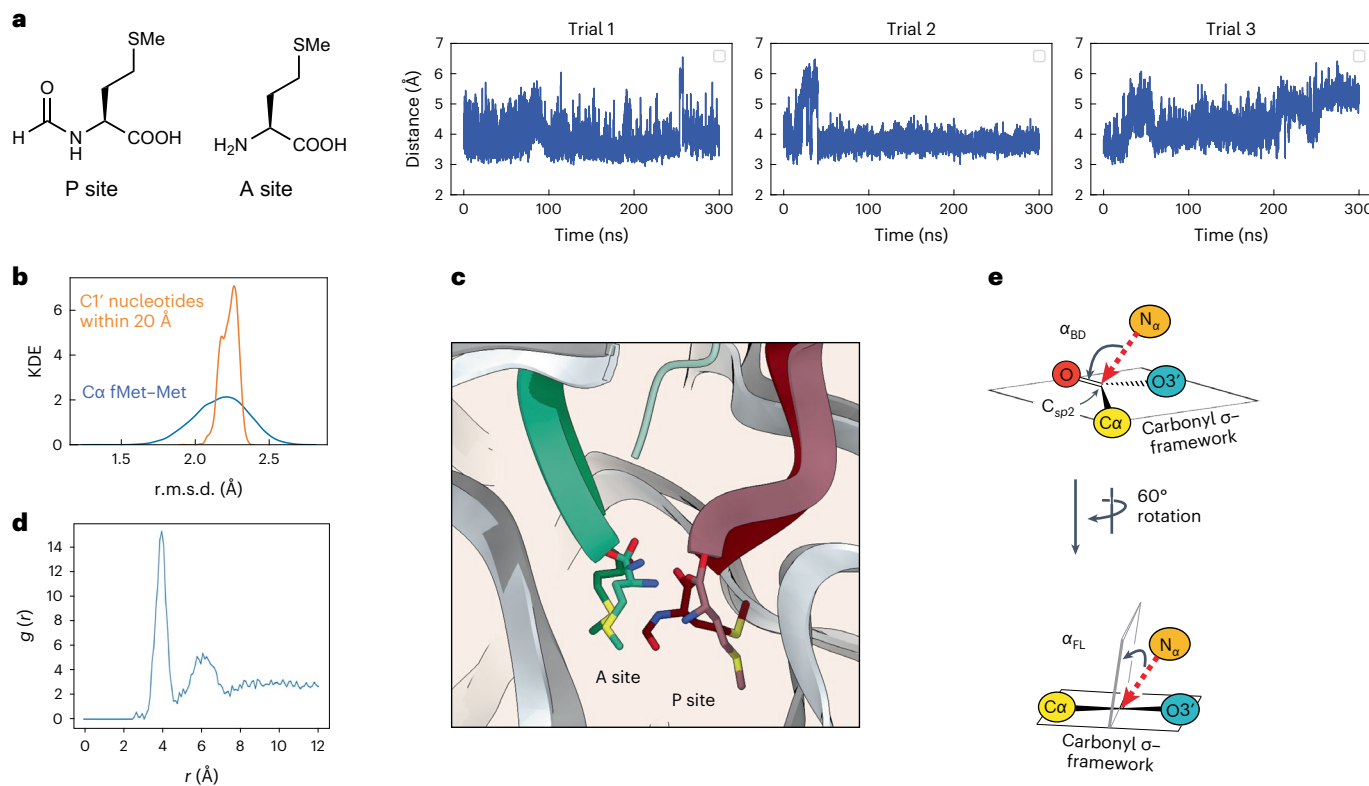


**Fig. 2 | MD simulations of the input fMet–Met ribosome structural model.** **a**, Trajectories illustrating the evolution of the distance between the A-site Met nucleophile ( $N_\alpha$ ) and the P-site fMet carbonyl electrophile ( $C_{sp2}$ ) over 300 ns within the 30 Å RRM. **b**, Kernel density estimation (KDE) of the r.m.s.d. of either the C1' nucleotides within the internal (non-fixed) 20 Å of the RRM (orange) or the C $\alpha$  carbons of Met and fMet (blue) over the course of the simulation. **c**, Close-up of the bond-forming region of the PTC in the 2.1 Å cryo-EM model reported here (lighter shades) and a representative pose (Methods) of the simulation

(darker shades) illustrating the relative positions of the Met and fMet monomers in the A and P sites, respectively. **d**, Radial distribution function  $g(r)$  indicates that the first and second solvation shells for the K $^+$  and Mg $^{2+}$  ions are within a distance ( $r$ ) of ~4 and 6 Å of the P atoms of residues C75 and A76, respectively. **e**, Illustration of the Bürgi–Dunitz angle ( $\alpha_{BD}$ ), which specifies the angle between the entering nucleophile and the  $C_{sp2}=O$  double bond, and the Flippin–Lodge angle ( $\alpha_{FL}$ ), which specifies the offset of the attack angle from the plane orthogonal to that defined by the carbonyl and the two adjacent substituents.  $\sigma$  = sigma.

improve the modelling of ordered water molecules, ions and polyamines in the PTC. Density for key bases U2506 and U2585 were modelled suboptimally in 7K00 due to poor density (Extended Data Fig. 1a), while in the current structure they have improved density best modelled in the favoured *anti* conformation in agreement with PDB 6XZ7 and 1VY4 (Extended Data Fig. 3a,b). The new map also enabled the modelling of residues 2–7 of bL27, the only ribosomal protein that is proximal to the tRNA CCA ends (Extended Data Fig. 3c).

Importantly for the simulations to follow, residues C75 and A76 in each acyl-tRNA are well resolved, with clear positioning of both the ribose and phosphate backbone as well as the amide linkages between Met and each A76 ribose (Fig. 1b). Beyond the amide linkage, the entirety of the A-site Met can be modelled. By contrast, the side chain and amine group of the P-site Met are not well resolved. However, the phosphate–ribose backbone of A76 in the P site is more clearly resolved than in previous models, resulting in a relative change in position (Extended Data Fig. 1c). In the model, the distance from the nucleophilic A-site amine  $N_\alpha$  to the P-site carbonyl carbon  $C_{sp2}$  is 3.3 Å (Fig. 1b,c). The ability to visualize these elements is especially important for simulations, in which some remaining details of the residues themselves would be substituted in silico. Additionally, the placement of these atoms is in good agreement with previously reported PDB 1VY4 (Extended Data Fig. 4), which contains fMet in the P site. Although formylation of the initial Met residue is thought to facilitate correct positioning of fMet via hydrogen bonding with G2061 of the 23S rRNA, and a similar hydrogen-bonding interaction is seen clearly in a recent nascent chain-containing structure<sup>34</sup>, relatively poor density

of the P-site monomer for both our map and 1VY4 suggests that a single Met residue in the P site remains disordered to some degree in the presence or absence of formylation.

#### Establishing a test system for simulation studies

It is a well-established approximation, when judiciously applied, that the truncation and/or constraining of distant atoms of the ribosome can reduce computational cost while still providing insight about conformational dynamics within the PTC<sup>35–37</sup>. We thus truncated the cryo-EM model reported here to include only those residues within 30 Å of both the A-site and P-site Met. This truncated model was solvated in a water box and a physiological concentration of KCl was added. As the simulation environment was set up with preliminary coordinates from the cryo-EM structure, which did not yet contain ions or spermidine ligands, ordered Mg $^{2+}$  ions from PDB 7K00 were rigid-body docked into the refined PTC coordinates. The final system contained ~88,000 atoms, including solvent, salt and counterions. This model is referred to as RRM, for the reduced ribosome model (Extended Data Fig. 5).

First, we set out to ensure that the RRM was stable during MD simulations and would recapitulate the conformations of the A-site and P-site monomers visualized by cryo-EM. We acylated the P-site Met with an *N*-formyl group in silico to serve as a more physiological initiator monomer, and positional restraints were placed on the C $\alpha$  of every ribosomal protein residue and the C1' of every nucleotide within the outer 10 Å of the 30 Å model. Test MD simulations (300 ns each) were run in triplicate, each with a different starting velocity, to

evaluate statistical uncertainties and improve sampling (Fig. 2a). As an initial validation step, we examined backbone atom fluctuations during the three 300 ns simulations with respect to the original cryo-EM structure. We evaluated both overall model stability (the root-mean-square deviation (r.m.s.d.) of every unrestrained C1' atom from its position in the cryo-EM structure) and monomer stability within the PTC (the r.m.s.d. of the Cα atoms of Met and fMet; Fig. 2b). Over the course of the simulation, the overall model r.m.s.d. was centred at 2.2 Å with a narrow distribution; stability within the PTC also averaged 2.2 Å, but with a slightly wider distribution. These metrics provide confidence that the overall RRM conformation and Met/fMet fluctuations remain stable (Fig. 2c).

As a further test of the validity of this model system, we examined the distribution of cations in the vicinity of the P-site tRNA 3'-CCA end. In the high-resolution structure determined here—after modelling of ions in the PTC was completed—and in the *Thermus thermophilus* structure (PDB 1VY4)<sup>24</sup>, a cation coordinates the phosphate group linking C75 and A76 of the P-site tRNA (Fig. 1b). Since the tRNA CCA ends were not well positioned in 7K00 (ref. 30), this Mg<sup>2+</sup> ion was not included in the initial RRM. Notably, in test MD simulations that included K<sup>+</sup> and Mg<sup>2+</sup> ions, strong cation positioning close to the P-site tRNA C75 and A76 phosphates is observed. The radial distribution functions for K<sup>+</sup> and Mg<sup>2+</sup> ions show ion to phosphorus distances consistent with phosphate coordination during the time course (Fig. 2d).

We next examined the geometric relationship between the A-site and P-site monomers that react to promote peptide bond formation. This geometric relationship is described by three metrics. The first is the distance between the candidate nucleophilic  $\alpha$ -amine of the A-site monomer ( $N_{\alpha}$ ) and the candidate electrophile, the ester carbonyl carbon of the P-site monomer ( $C_{sp2}$ ). This  $N_{\alpha}$ – $C_{sp2}$  distance is 3.3 Å in the 2.1-Å-resolution cryo-EM structure reported here; it averaged  $4.0 \pm 0.3$  Å throughout the three simulations. The second and third metrics are angles that define the approach of the nucleophile relative to the carbonyl (Fig. 2e). The Bürgi–Dunitz angle ( $\alpha_{BD}$ )<sup>32</sup> specifies the angle between the entering nucleophilic  $N_{\alpha}$  and the  $C_{sp2}$ =O double bond. Reported values<sup>32,38</sup> for  $\alpha_{BD}$  vary from  $-105^\circ$  to  $-90^\circ$ . The Flippin–Lodge angle ( $\alpha_{FL}$ )<sup>39,40</sup> specifies the offset of the attack angle from the plane orthogonal to that defined by the carbonyl and the two adjacent substituents and is smaller, often  $<20^\circ$ . The values of  $\alpha_{BD}$  and  $\alpha_{FL}$  derived from the cryo-EM structure reported here are  $98^\circ$  and  $19^\circ$ , respectively, also in line with canonical data and predictions. The average values of  $\alpha_{BD}$  and  $\alpha_{FL}$  derived from the simulations are centred at  $94^\circ \pm 15^\circ$  and  $38^\circ \pm 12^\circ$ , respectively.

### Evaluation of non-L- $\alpha$ -amino acid monomers

With a validated workflow in hand, we evaluated the intra-PTC conformational landscapes of two sets of non-L- $\alpha$ -amino acid monomers (Fig. 3). These monomers exhibit differences in overall structure, stereochemistry and basicity of the nucleophilic atom. All the monomers acylate a common tRNA with a high yield in flexizyme (ref. 41)-promoted reactions, yet within a given set, the acylated tRNAs that result differ substantially in translational efficiency in vitro using *E. coli* ribosomes. The first monomer set comprises a trio of aminobenzoic acid derivatives (2–4) that introduce extended,  $sp^2$ -hybridized aromatic backbones into translated polypeptides. Of these three monomers, *ortho*-substituted pyridine 2 is the most reactive, with a translation yield at least fourfold higher than reactions of tRNA acylated with *ortho*-aminobenzoic acid 3 (ref. 13). The translation yield using *meta*-aminobenzoic acid 4 was almost undetectable. The second monomer set comprises all four stereoisomers of the cyclic  $\beta^{2,3}$ -amino acid 2-aminocyclopentane-1-carboxylic acid (5–8) (ref. 10), studied extensively as foldamers<sup>42</sup>. Of these four monomers, stereoisomer 5 is the most reactive; the translation yield was more than tenfold higher than that of enantiomer 8. The translational efficiencies of the enantiomeric pair 6 and 7 were moderate.

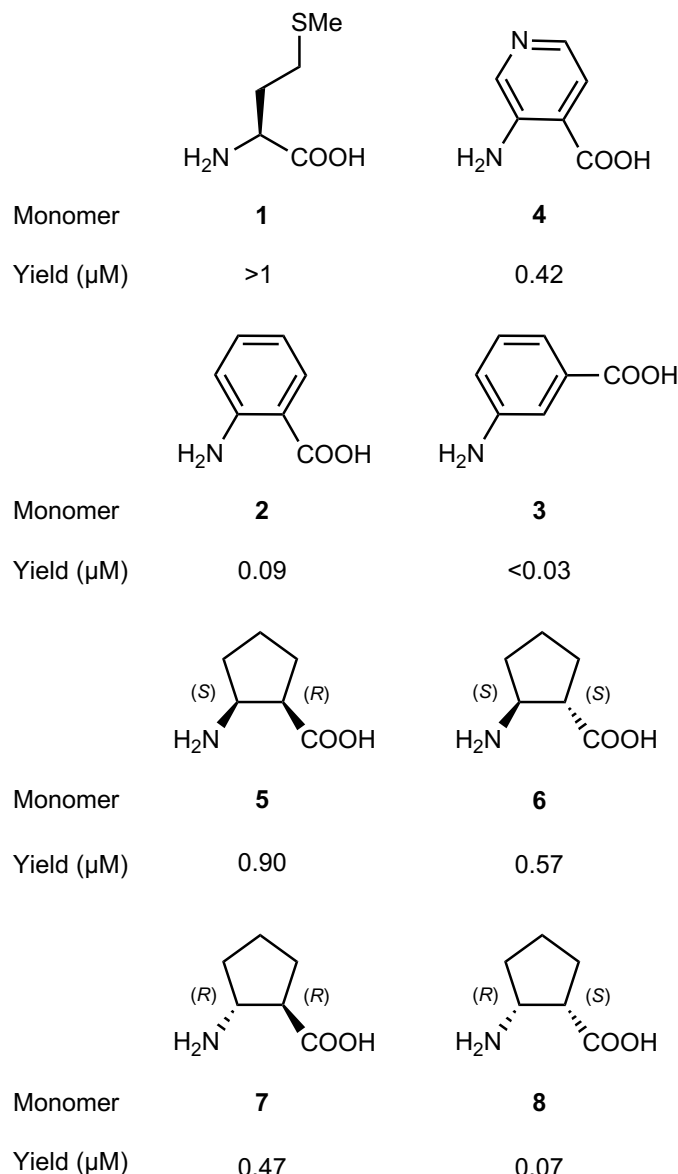


**Fig. 3 | Chemical structures of monomers tested in MD and meta-dynamics simulations.** Structures of aminobenzoic acid and cyclic  $\beta^{2,3}$ -2-aminocyclopentane-1-carboxylic acid monomers and data from in vitro translation assays are shown. The yield shown represents the relative efficiency of translation of DNA template fMet-Trp-Lys-Trp-Lys-Trp-Lys-X-Gly-Asp-Tyr-Lys-Asp-Asp-Asp-Lys (for aminobenzoic acids) or fMet-Trp-Lys-Trp-Lys-Lys-Trp-Lys-Phe-X-Gly-Asp-Tyr-Lys-Asp-Asp-Asp-Asp-Lys (for cyclic  $\beta^{2,3}$ -2-aminocyclopentane-1-carboxylic acid monomers). In vitro translation reaction conditions were comparable within each monomer class, as was the efficiency of tRNA acylation. Because the templates differ, comparisons are limited to those within a given monomer class. The value for Met was estimated at 2.5 times the efficiency of Ala.

### $N_{\alpha}$ – $C_{sp2}$ distance is not a predictor of reactivity

Next, we evaluated in triplicate the evolution of each non-L- $\alpha$ -amino acid monomer over 300 ns within the PTC of the 30 Å RRM. We evaluated changes in the distance between  $N_{\alpha}$  and  $C_{sp2}$  as well as the values of  $\alpha_{BD}$  and  $\alpha_{FL}$  (Fig. 4 and Extended Data Fig. 6). A plot of the average kernel density estimate as a function of all three metrics spans a wide range for both monomer sets (Fig. 4a). As described above, simulation of the native fMet–Met pair reproduces the expected values for the  $N_{\alpha}$ – $C_{sp2}$  distance ( $4.0 \pm 0.3$  Å) and reasonable values of both  $\alpha_{BD}$  ( $94^\circ \pm 15^\circ$ ) and  $\alpha_{FL}$  ( $38^\circ \pm 12^\circ$ ). However, the midpoint  $N_{\alpha}$ – $C_{sp2}$

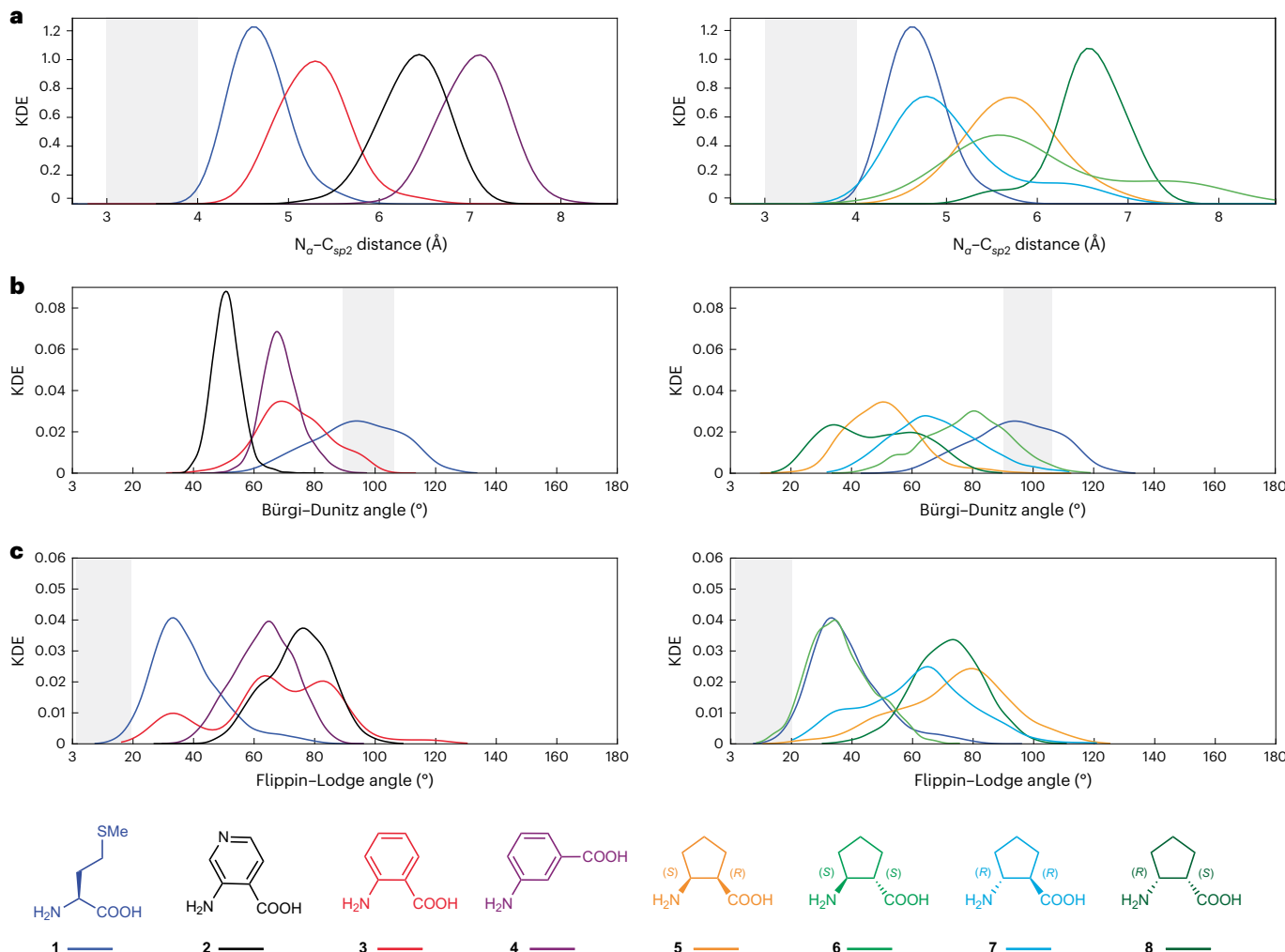


**Fig. 4 | Kernel density estimation of the three geometric measurements from MD simulations.** **a–c**,  $N_{\alpha}$ –C<sub>sp2</sub> distance (a), Bürgi–Dunitz angle (b) and Flippin–Lodge angle (c) for aminobenzoic acids (left) and  $\beta^{2,3}$ -amino acid 2-aminocyclopentane-1-carboxylic acid monomers (right) within the RRM over

the course of the 300 ns simulation. The grey zones highlight  $N_{\alpha}$ –C<sub>sp2</sub> distances of between 3 and 4 Å, and values of  $\alpha_{BD}$  and  $\alpha_{FL}$  between 90° to 105° and 5° to 20°, respectively.

distance for non-L- $\alpha$ -amino acid monomers **2–8** does not correlate with reactivity. For aminobenzoic acids **2–4**, although the midpoint  $N_{\alpha}$ –C<sub>sp2</sub> distance for *ortho*-aminobenzoic acid **3** (4.7 Å) is smaller than that of *meta*-aminobenzoic acid **4** (6.4 Å), it is also smaller than that of the pyridine analogue **2** (5.7 Å), which is by far the most reactive in this monomer set. In the case of cyclic  $\beta^{2,3}$ -amino acids, reactivity again fails to track with midpoint  $N_{\alpha}$ –C<sub>sp2</sub> distance. Reactivity tracks in the order **5 > 6 ≈ 7 ≈ 8**, whereas the midpoint  $N_{\alpha}$ –C<sub>sp2</sub> distance tracks in the order **7 < 5 ≈ 6 < 8**. Similar conclusions can be drawn when  $\alpha_{BD}$  and  $\alpha_{FL}$  are considered in place of the midpoint  $N_{\alpha}$ –C<sub>sp2</sub> distance (Fig. 4b,c and Extended Data Fig. 7).

### Metadynamics widely samples intra-PTC monomer conformation

Based on the lack of correlation discussed above, we concluded that in the absence of experimentally determined starting structures for non-L- $\alpha$ -amino acid monomers, the in silico assembled starting conformations could be trapped in local energy wells and likely did not explore the entirety of conformational space during the course of the MD simulation. This problem is common in MD simulations of biomolecular systems—sometimes the sampling over a given time scale is insufficient, whereas at other times the system may be trapped at a

local energy minimum and diffuse slowly, and at still other times both of these scenarios occur simultaneously<sup>27,43,44</sup>. To achieve a more thorough sampling of the monomer-dependent conformational landscape within the PTC, we turned to metadynamics<sup>45</sup>, which has been used extensively in the sampling of biomolecular simulations<sup>46</sup>. Metadynamics improves sampling by introducing an additional force (bias potential) on a chosen number of and chosen types of degrees of freedom known as collective variables. For practical purposes, it is important to limit the number of collective variables, while choosing collective variables that efficiently sample the desirable conformational space<sup>47,48</sup>. We thus chose two collective variables: the  $N_{\alpha}$ –C<sub>sp2</sub> distance and the  $\alpha_{BD}$  value. The  $\alpha_{BD}$  value was chosen in preference to  $\alpha_{FL}$  because it varies over a wider range among the monomers evaluated (Extended Data Fig. 7).

### Metadynamics recapitulates monomer relative reactivity

We began the metadynamics simulations with two initial conformations of each monomer. One conformation was identical to that used to initiate unbiased MD simulations (Fig. 4). The second conformation was altered by rotating the psi ( $\psi$ ) angle (angle between the C $\alpha$  and the C<sub>sp2</sub> of the monomers) by 180°, to generate an alternative initial position of the nucleophile amine  $N_{\alpha}$  relative to the C<sub>sp2</sub> of fMet. Examination of plots showing  $\alpha_{BD}$  as a function of the  $N_{\alpha}$ –C<sub>sp2</sub> distance after the

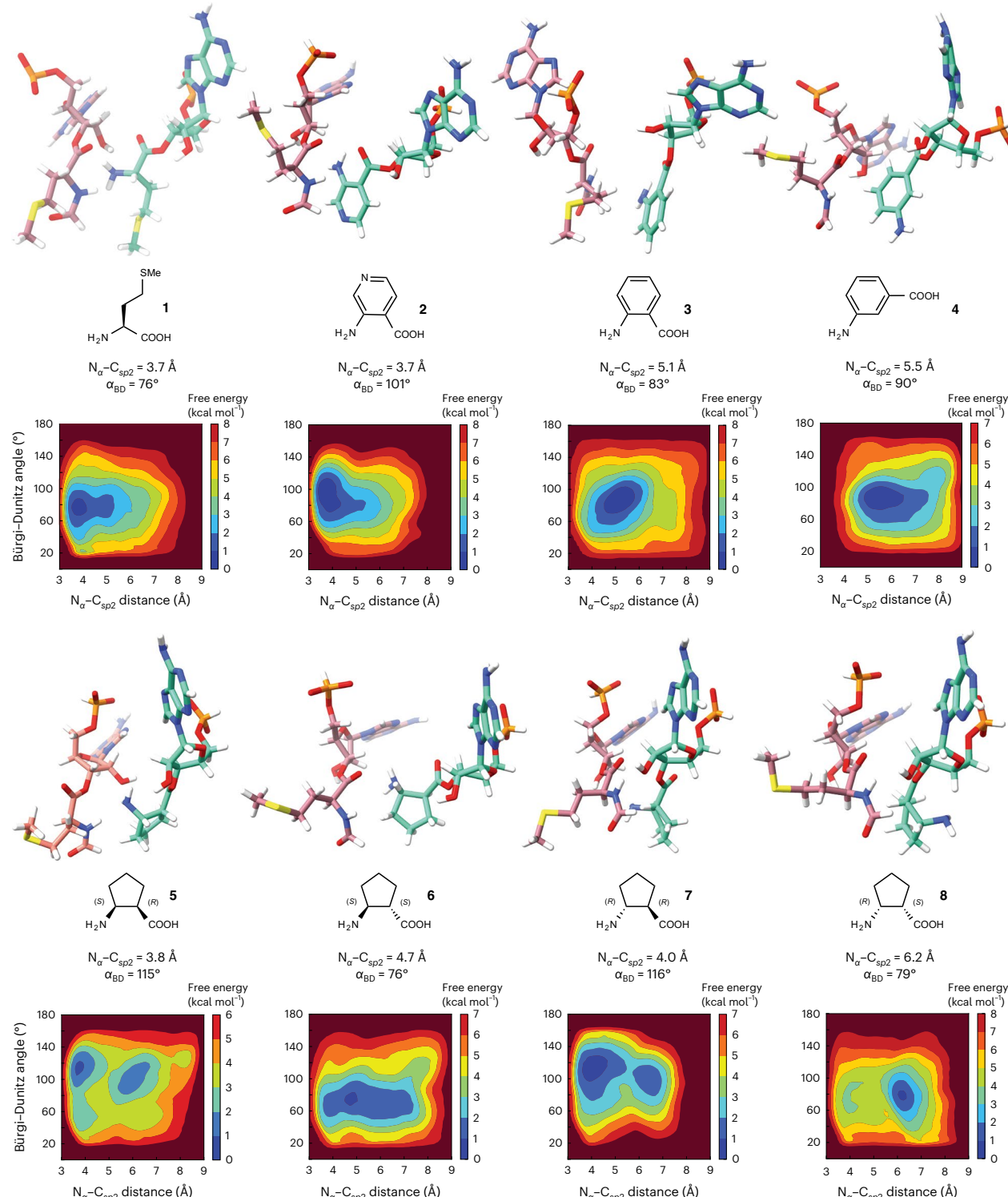


**Fig. 5 | Plots of FESs from metadynamics simulations.** FESs of 30 Å RRM containing a P-site tRNA acylated with fMet and A-site tRNAs acylated with monomers **1–8**, plotted along the collective variables of Bürgi–Dunitz angle  $\alpha_{BD}$  and  $N_{\alpha}-C_{sp^2}$  distance. The metadynamics simulations that generated each FES began with the 2.1 Å cryo-EM model reported here, but the A-site Met was in silico mutated to the other monomers, while the P-site Met was converted to fMet. Each FES shown is the average of two metadynamics runs starting from orientations of the A-site monomers that differ by a 180° rotation about the  $\psi$  angle. The colour scale represents the free energy in kilocalories per mole, where the global minima are set at 0 and therefore the various heights of the energy scales are based on the energetics of the fluctuations of the A-site monomers. The conformation and relative geometry of the P-site (rose) and A-site (green) monomers at the free energy minimum are shown above each plot. Poses were chosen to highlight the

$N_{\alpha}-C_{sp^2}$  distance and the Bürgi–Dunitz angle  $\alpha_{BD}$  at the free energy minimum. The tRNAs to which each monomer is attached as well as the RRM surrounding the two monomers have been omitted for clarity. Coordinates for the lowest energy models obtained for each simulation are available at <https://doi.org/10.5281/zenodo.7730661>. Two methods were used to establish that convergence was reached during the 100 ns runs. First, trajectory plots representing the  $N_{\alpha}-C_{sp^2}$  distance and Bürgi–Dunitz angle ( $\alpha_{BD}$ ) for metadynamics replicas reveal that the conformation space is revisited multiple times over the course of the metadynamics runs (Supplementary Figs. 2 and 3). Second, FESs calculated for the last 80 ns of the 100 ns simulation are qualitatively similar to those calculated after 100 ns, with the differences between the FESs of the last 80 ns and after 100 ns on average  $-0.8$  kcal mol $^{-1}$  (Supplementary Figs. 4–6).

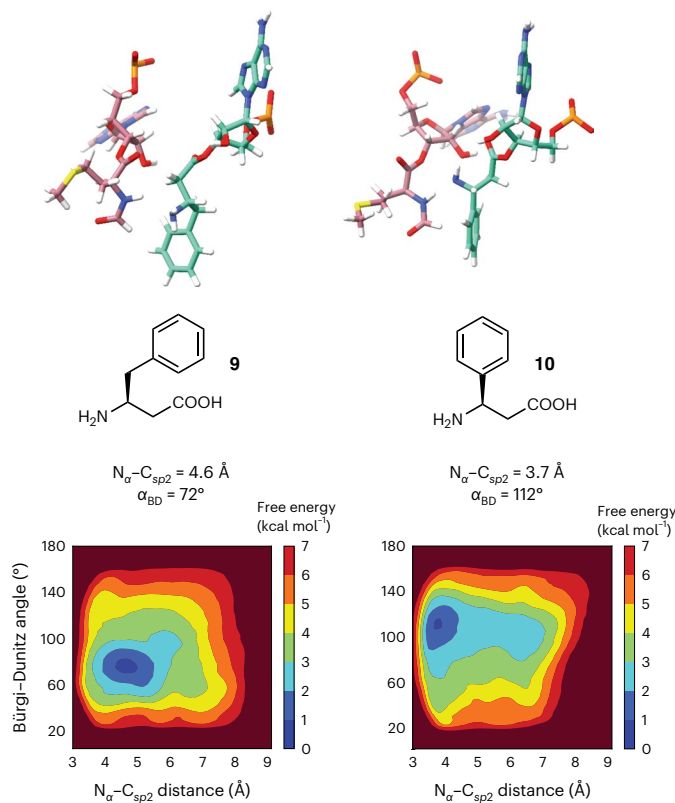


**Fig. 6 | Metadynamics analysis of structurally unrelated monomers.**  
The workflow accurately predicts the relative reactivities of two monomers that are structurally unrelated to monomers **2–8**, notably the less reactive (S)- $\beta^3$ -homophenylalanine **9** and the more reactive (S)- $\beta^3$ -homophenylglycine **10**. Shown are the FESs produced by the metadynamics workflow as well as the poses and geometries of the two systems at the global minimum.

metadynamics simulations reveals minima that clearly differentiate highly reactive and less reactive monomers within each monomer set (Fig. 5). The metadynamics free energy surface (FES) contour plot of a RRM containing P-site fMet and A-site Met monomers shows excellent agreement with the  $N_\alpha$ -C<sub>sp2</sub> distance and  $\alpha_{BD}$  values determined by cryo-EM. The global minimum  $N_\alpha$ -C<sub>sp2</sub> distance is centred at 3.7 Å, and the global minimum value of  $\alpha_{BD}$  is centred at 76°, while the fluctuations within 1 kcal mol<sup>-1</sup> reach values between 3.4–4.4 Å and 61–90°, respectively. These values show good agreement with both unbiased MD results (4 Å and 94°) and the metrics derived from the high-resolution structure reported here (3.3 Å and 93°).

More importantly, the global minima for the monomer within each set that reacts most efficiently within the PTC, notably pyridine **2** and (1*R*,2*S*)-2-aminocyclopentane carboxylic acid **5**, populate conformations within the PTC with  $N_\alpha$ -C<sub>sp2</sub> distances centred at or below 3.8 Å and  $\alpha_{BD}$  values between 101° and 115°. By contrast, monomers that are relatively inactive, notably *ortho*- and *meta*-aminobenzoic acids **3** and **4** and (1*S*,2*R*)-2-aminocyclopentane carboxylic acid **8** (the enantiomer of **5**), populate conformations with  $N_\alpha$ -C<sub>sp2</sub> distances between 5.1 and 6.2 Å, with  $\alpha_{BD}$  values centred at 84°. The two moderately active 2-aminocyclopentane carboxylic acid isomers **6** and **7** populate a conformational space defined by either long  $N_\alpha$ -C<sub>sp2</sub> distances (**6**) or dual conformational minima (**7**).

We also carried out additional metadynamics simulations of the RRM in which the P-site monomer was Met (not fMet) and the A-site monomer was either aminobenzoic acid **2** (highly reactive) or aminobenzoic acid **4** (poorly reactive; Extended Data Fig. 8c–f). In this case, when the simulations begin without an *N*-formyl group, monomer

**4** shows a more significant change in its FES than does monomer **2**. As a result, monomer **4** shows a more favourable energy minimum (in terms of distance) for the reaction to occur, and the differences between the minimum energy poses are not as large as when the simulation begins with an N-terminal fMet. This result provides additional support for our decision to formylate the P-site Met in silico prior to initiating simulation. Regardless, these data suggest that the most reactive aramid monomers significantly populate a conformational space characterized by an average  $N_\alpha$ -C<sub>sp2</sub> distance of <4 Å and an average  $\alpha_{BD}$  of between 76° and 115°.

Encouraged by these results, we next asked whether we could apply the metadynamics workflow to classify the relative reactivities of two structurally unrelated monomers that possess greater conformational freedom than those evaluated initially—notably (S)- $\beta^3$ -homophenylalanine **9** and (S)- $\beta^3$ -homophenylglycine **10**. These monomers acylate an identical tRNA with identical efficiencies in flexizyme-promoted reactions, but (S)- $\beta^3$ -homophenylglycine **10** is noticeably more reactive in *in vitro* translation reactions<sup>49</sup>. Application of the metadynamics workflow outlined above for monomers **2–8** to monomers **9** and **10** generated a pair of FESs that clearly differentiated the two monomers in a manner consistent with their reactivity (Fig. 6). The global minimum of the FES generated for a RRM containing monomer **10** in the A site mirrors that of reactive monomers **2** and **5**, notably a  $N_\alpha$ -C<sub>sp2</sub> distance centred at or below 4 Å (3.7 Å) and  $\alpha_{BD}$  of 111°. By contrast, the global minimum for monomer **9** mirrors that for inactive monomer **4**, notably a  $N_\alpha$ -C<sub>sp2</sub> distance greater than 4.6 Å and a low  $\alpha_{BD}$  of 72°.

## Conclusions

In summary, here we implement a structure-informed, physics-based workflow to reliably classify the reactivity of non-L- $\alpha$ -amino acid monomers in amide-bond-forming reactions catalysed by the *E. coli* ribosome. Non-L- $\alpha$ -amino acid monomers that populate a conformational space characterized by  $N_\alpha$ -C<sub>sp2</sub> distances of ≤4 Å and Bürgi-Dunitz angles of 76° and 115° react efficiently within the PTC of wild-type *E. coli* ribosomes. These predictions hold for three diverse families of molecules: aminobenzoic acids,  $\beta^3$ -amino acids and  $\beta^{2,3}$ -cyclic amino acids. Monomers that cannot appreciably occupy a region in which the  $N_\alpha$ -C<sub>sp2</sub> distance is less than 4 Å, even with an acceptable Bürgi-Dunitz angle, do not react. The experimental data, along with the models that emerge from the simulations, are both consonant with notions about ‘near-attack/near in-line attack’ transition states in biocatalysis<sup>50</sup>. Importantly, these bond-forming trajectories intersect with the stereoelectronic considerations associated with our analysis of Bürgi-Dunitz ( $\alpha_{BD}$ ) and Flippin-Lodge ( $\alpha_{FL}$ ) angles. Accordingly, even in the absence of a high-level quantum mechanical treatment of these in-ribosome transition states, the convergence of the experimental data and simulations with the observed incorporation efficiencies of natural and non-natural non-L- $\alpha$ -amino monomers provides a self-consistent picture of accessible geometries for efficient incorporation. More broadly, the metadynamics workflow implemented herein addresses two barriers impeding the ribosome-promoted biosynthesis of diverse heterooligomers. For applications *in vivo*, metadynamics can prioritize monomers for which orthogonal aminoacyl-tRNA synthetase variants are needed. For applications *in vitro*, metadynamics can identify monomers that are likely to react within the PTC of wild-type ribosomes, and those for which engineered ribosomes are needed.

## Online content

Any methods, additional references, Nature Portfolio reporting summaries, source data, extended data, supplementary information, acknowledgements, peer review information; details of author contributions and competing interests; and statements of data and code availability are available at <https://doi.org/10.1038/s41557-023-01226-w>.

## References

1. Liu, C. & Schultz, P. in *Annual Review of Biochemistry* (eds Kornberg, R., Raetz, C., Rothman, J. & Thorner, J.) **79**, 413–444 (Annual Reviews, 2010).
2. Czekster, C. M., Robertson, W. E., Walker, A. S., Soell, D. & Schepartz, A. *In vivo* biosynthesis of a beta-amino acid-containing protein. *J. Am. Chem. Soc.* **138**, 5194–5197 (2016).
3. Chen, S., Ji, X., Gao, M., Dedkova, L. M. & Hecht, S. M. *In cellulo* synthesis of proteins containing a fluorescent oxazole amino acid. *J. Am. Chem. Soc.* **141**, 5597–5601 (2019).
4. Guo, J., Wang, J., Anderson, J. C. & Schultz, P. G. Addition of an  $\alpha$ -hydroxy acid to the genetic code of bacteria. *Angew. Chem. Int. Ed.* **47**, 722–725 (2008).
5. Kobayashi, T., Yanagisawa, T., Sakamoto, K. & Yokoyama, S. Recognition of non- $\alpha$ -amino substrates by pyrrolysyl-tRNA synthetase. *J. Mol. Biol.* **385**, 1352–1360 (2009).
6. England, P. M., Zhang, Y., Dougherty, D. A. & Lester, H. A. Backbone mutations in transmembrane domains of a ligand-gated ion channel: implications for the mechanism of gating. *Cell* **96**, 89–98 (1999).
7. Spinck, M. et al. Genetically programmed cell-based synthesis of non-natural peptide and depsipeptide macrocycles. *Nat. Chem.* **15**, 61–69 (2023).
8. Ad, O. et al. Translation of diverse aramid- and 1,3-dicarbonyl-peptides by wild type ribosomes *in vitro*. *ACS Cent. Sci.* **5**, 1289–1294 (2019).
9. Takatsuji, R. et al. Ribosomal synthesis of backbone-cyclic peptides compatible with *in vitro* display. *J. Am. Chem. Soc.* **141**, 2279–2287 (2019).
10. Katoh, T., Sengoku, T., Hirata, K., Ogata, K. & Suga, H. Ribosomal synthesis and *de novo* discovery of bioactive foldamer peptides containing cyclic  $\beta$ -amino acids. *Nat. Chem.* **12**, 1081–1088 (2020).
11. Katoh, T. & Suga, H. Ribosomal elongation of cyclic  $\gamma$ -amino acids using a reprogrammed genetic code. *J. Am. Chem. Soc.* **142**, 4965–4969 (2020).
12. Lee, J., Schwarz, K. J., Kim, D. S., Moore, J. S. & Jewett, M. C. Ribosome-mediated polymerization of long chain carbon and cyclic amino acids into peptides *in vitro*. *Nat. Commun.* **11**, 4304 (2020).
13. Katoh, T. & Suga, H. Ribosomal elongation of aminobenzoic acid derivatives. *J. Am. Chem. Soc.* **142**, 16518–16522 (2020).
14. Adaligil, E., Song, A., Hallenbeck, K. K., Cunningham, C. N. & Fairbrother, W. J. Ribosomal synthesis of macrocyclic peptides with  $\beta^2$ - and  $\beta^{2,3}$ -homo-amino acids for the development of natural product-like combinatorial libraries. *ACS Chem. Biol.* **16**, 1011–1018 (2021).
15. Katoh, T. & Suga, H. Consecutive ribosomal incorporation of  $\alpha$ -aminoxy/ $\alpha$ -hydrazino acids with L/D-configurations into nascent peptide chains. *J. Am. Chem. Soc.* **143**, 18844–18848 (2021).
16. Sievers, A., Beringer, M., Rodnina, M. V. & Wolfenden, R. The ribosome as an entropy trap. *Proc. Natl Acad. Sci. USA* **101**, 7897–7901 (2004).
17. Whitford, P. C., Blanchard, S. C., Cate, J. H. D. & Sanbonmatsu, K. Y. Connecting the kinetics and energy landscape of tRNA translocation on the ribosome. *PLoS Comput. Biol.* **9**, e1003003 (2013).
18. Trabuco, L. G., Harrison, C. B., Schreiner, E. & Schulten, K. Recognition of the regulatory nascent chain TnAC by the ribosome. *Structure* **18**, 627–637 (2010).
19. Trylska, J., Tozzini, V. & McCammon, J. A. Exploring global motions and correlations in the ribosome. *Biophys. J.* **89**, 1455–1463 (2005).
20. Tama, F., Valle, M., Frank, J. & Brooks, C. L. Dynamic reorganization of the functionally active ribosome explored by normal mode analysis and cryo-electron microscopy. *Proc. Natl Acad. Sci. USA* **100**, 9319–9323 (2003).
21. Wang, Y., Rader, A. J., Bahar, I. & Jernigan, R. L. Global ribosome motions revealed with elastic network model. *J. Struct. Biol.* **147**, 302–314 (2004).
22. Kazemi, M., Socan, J., Himo, F. & Åqvist, J. Mechanistic alternatives for peptide bond formation on the ribosome. *Nucleic Acids Res.* **46**, 5345–5354 (2018).
23. Cech, T. R. Structural biology. The ribosome is a ribozyme. *Science* **289**, 878–879 (2000).
24. Polikanov, Y. S., Steitz, T. A. & Innis, C. A. A proton wire to couple aminoacyl-tRNA accommodation and peptide-bond formation on the ribosome. *Nat. Struct. Mol. Biol.* **21**, 787–793 (2014).
25. Gorbachev, V., Tsybizova, A., Miloglyadova, L. & Chen, P. Increasing complexity in a conformer space step-by-step: weighing London dispersion against cation– $\pi$  interactions. *J. Am. Chem. Soc.* **144**, 9007–9022 (2022).
26. Miao, Z. et al. RNA-puzzles round IV: 3D structure predictions of four ribozymes and two aptamers. *RNA* **26**, 982–995 (2020).
27. Bottaro, S. & Lindorff-Larsen, K. Biophysical experiments and biomolecular simulations: a perfect match? *Science* **361**, 355–360 (2018).
28. Šponer, J. et al. RNA structural dynamics as captured by molecular simulations: a comprehensive overview. *Chem. Rev.* **118**, 4177–4338 (2018).
29. Frye, L., Bhat, S., Akinsanya, K. & Abel, R. From computer-aided drug discovery to computer-driven drug discovery. *Drug Discov. Today Technol.* **39**, 111–117 (2021).
30. Watson, Z. L. et al. Structure of the bacterial ribosome at 2 Å resolution. *eLife* **9**, e60482 (2020).
31. Pichkur, E. B. et al. Insights into the improved macrolide inhibitory activity from the high-resolution cryo-EM structure of dirithromycin bound to the *E. coli* 70S ribosome. *RNA* **26**, 715–723 (2020).
32. Bürge, H. B., Dunitz, J. D., Lehn, J. M. & Wipff, G. Stereochemistry of reaction paths at carbonyl centres. *Tetrahedron* **30**, 1563–1572 (1974).
33. Gamper, H. & Hou, Y.-M. tRNA 3'-amino-tailing for stable amino acid attachment. *RNA* **24**, 1878–1885 (2018).
34. Syroegin, E. A., Aleksandrova, E. V. & Polikanov, Y. S. Insights into the ribosome function from the structures of non-arrested ribosome-nascent chain complexes. *Nat. Chem.* **15**, 143–153 (2022).
35. Chirkova, A. et al. The role of the universally conserved A2450–C2063 base pair in the ribosomal peptidyl transferase center. *Nucleic Acids Res.* **38**, 4844–4855 (2010).
36. Makarov, G. I., Golovin, A. V., Sumbatyan, N. V. & Bogdanov, A. A. Molecular dynamics investigation of a mechanism of allosteric signal transmission in ribosomes. *Biochem. (Moscow)* **80**, 1047–1056 (2015).
37. Englander, M. T. et al. The ribosome can discriminate the chirality of amino acids within its peptidyl-transferase center. *Proc. Natl Acad. Sci. USA* **112**, 6038–6043 (2015).
38. Radisky, E. S. & Koshland, D. E. A clogged gutter mechanism for protease inhibitors. *Proc. Natl Acad. Sci. USA* **99**, 10316–10321 (2002).
39. Heathcock, C. H. & Flippin, L. A. Acyclic stereoselection. 16. High diastereofacial selectivity in Lewis acid mediated additions of enol silanes to chiral aldehydes. *J. Am. Chem. Soc.* **105**, 1667–1668 (1983).
40. Lodge, E. P. & Heathcock, C. H. Acyclic stereoselection. 40. Steric effects, as well as  $\sigma^*$ -orbital energies, are important in diastereoface differentiation in additions to chiral aldehydes. *J. Am. Chem. Soc.* **109**, 3353–3361 (1987).
41. Ramaswamy, K., Saito, H., Murakami, H., Shiba, K. & Suga, H. Designer ribozymes: programming the tRNA specificity into flexizyme. *J. Am. Chem. Soc.* **126**, 11454–11455 (2004).
42. Choi, S. H., Guzel, I. A. & Gellman, S. H. Crystallographic characterization of the  $\alpha$ / $\beta$ -peptide 14/15-helix. *J. Am. Chem. Soc.* **129**, 13780–13781 (2007).

43. Bernardi, R. C., Melo, M. C. R. & Schulten, K. Enhanced sampling techniques in molecular dynamics simulations of biological systems. *Biochim. Biophys. Acta* **1850**, 872–877 (2015).
44. Invernizzi, M., Piaggi, P. M. & Parrinello, M. Unified approach to enhanced sampling. *Phys. Rev. X* **10**, 041034 (2020).
45. Laio, A. & Parrinello, M. Escaping free-energy minima. *Proc. Natl Acad. Sci. USA* **99**, 12562–12566 (2002).
46. Pfaendtner, J. Metadynamics to enhance sampling in biomolecular simulations. *Methods Mol. Biol.* **2022**, 179–200 (2019).
47. Barducci, A., Bonomi, M. & Parrinello, M. Metadynamics. *WIREs Comput. Mol. Sci.* **1**, 826–843 (2011).
48. Bussi, G. & Laio, A. Using metadynamics to explore complex free-energy landscapes. *Nat. Rev. Phys.* **2**, 200–212 (2020).
49. Fujino, T., Goto, Y., Suga, H. & Murakami, H. Ribosomal synthesis of peptides with multiple  $\beta$ -amino acids. *J. Am. Chem. Soc.* **138**, 1962–1969 (2016).
50. Torres, R. A. & Bruice, T. C. Molecular dynamics study displays near in-line attack conformations in the hammerhead ribozyme self-cleavage reaction. *Proc. Natl Acad. Sci. USA* **95**, 11077–11082 (1998).

**Publisher's note** Springer Nature remains neutral with regard to jurisdictional claims in published maps and institutional affiliations.

**Open Access** This article is licensed under a Creative Commons Attribution 4.0 International License, which permits use, sharing, adaptation, distribution and reproduction in any medium or format, as long as you give appropriate credit to the original author(s) and the source, provide a link to the Creative Commons license, and indicate if changes were made. The images or other third party material in this article are included in the article's Creative Commons license, unless indicated otherwise in a credit line to the material. If material is not included in the article's Creative Commons license and your intended use is not permitted by statutory regulation or exceeds the permitted use, you will need to obtain permission directly from the copyright holder. To view a copy of this license, visit <http://creativecommons.org/licenses/by/4.0/>.

© The Author(s) 2023

## Methods

### Preparation of acylated tRNA

**Synthesis of N-1 tRNA<sup>fMet</sup>.** tRNAs missing the 3' terminal nucleotide are referred to here as N-1 tRNAs'. Templates for in vitro transcription were prepared using a double polymerase chain reaction (PCR) amplification method. Base C1 was mutated to G for optimal T7 RNA polymerase initiation. First, long overlapping primers tRNA-fMet-C1G\_temp F and RNA-fMet-C1G\_A\_temp R (Supplementary Table 1) were PCR amplified using Q5 DNA polymerase from New England Biolabs (NEB). Products were gel purified and amplified using short primers tRNA-fMet-C1G\_amp F and tRNA-fMet-C1G\_A\_amp R (Supplementary Table 1). The second base of each reverse primer in this step was modified with 2'OMe to prevent nonspecific addition by T7 RNA polymerase<sup>51</sup>. Amplification PCRs were  $\times 1$  phenol chloroform extracted,  $\times 2$  chloroform washed and precipitated with  $\times 3$  volumes of ethanol (EtOH). DNA quantity was measured on an agarose gel using a known standard.

T7 in vitro transcription was performed in a buffer containing 50 mM Tris-HCl, pH 7.5; 15 mM MgCl<sub>2</sub>; 5 mM dithiothreitol (DTT); and 2 mM spermidine. Reactions contained 2.5 mM each nucleoside triphosphate (NTP), 1:40 NEB murine RNase inhibitor, 25  $\mu$ g T7 RNA polymerase (gift from B. Martinez, Cate Lab), 0.0005 U  $\mu$ l<sup>-1</sup> pyrophosphatase (PPase) and  $\sim$ 1,000 ng DNA template per 100  $\mu$ l of transcription reaction. Reactions were incubated for 16 h at 37 °C; treated with 1/20th volume RQ1 deoxyribonuclease (DNase; 1 U  $\mu$ l<sup>-1</sup> stock) for 30 min at 37 °C; and precipitated with 1/10th volume of 3 M NaOAc, pH 5.2, and  $\times 3$  volumes of EtOH. Precipitated tRNA was pelleted, washed once with 70% EtOH and resuspended in loading dye (95% formamide, 40 mM EDTA, 0.05% bromophenol blue, 0.05% xylene cyanol).

Gel purification was performed using  $\sim$ 20-cm-long 12% polyacrylamide  $\times 1$  TBE 7 M urea gels poured roughly 2 mm thick. Bands were excised using UV shadowing, crushed, frozen on dry ice briefly (with elution buffer) and eluted at 4 °C overnight in 300 mM NaOAc, pH 5.2; 1 mM EDTA; and 0.5% (w/v) sodium dodecyl sulfate (SDS). Approximately 2 ml buffer was used per 500  $\mu$ l transcription reaction. Eluted tRNA was pipetted off the gel debris and precipitated with 1  $\mu$ l GlycoBlue Coprecipitant and  $\times 3$  volumes of EtOH. Pelleted tRNA was resuspended in water and stored at  $\sim$ 80 °C.

**Purification of *Archaeoglobus fulgidus* CCA-adding enzyme.** The full CCA-adding enzyme gene was purchased from Twist Bioscience and cloned into a plasmid carrying a T7 promoter and C-terminal 6x histidine tag. The resulting plasmid was transformed into BL21 (DE3) Rosetta2 pLysS cells for expression. Some 2  $\times$  1 l of lysogeny broth (LB) + 100  $\mu$ g ml<sup>-1</sup> ampicillin were induced with a 1:100 dilution of overnight culture (grown at 37 °C). Cells were grown at 37 °C until the optical density measured at a wavelength of 600 nm (OD<sub>600</sub>) was  $\sim$ 0.5, and induced with 0.5 mM isopropylthio- $\beta$ -galactoside (IPTG) for 3 h. Cells were pelleted and washed with lysis buffer (20 mM HEPES buffer, pH 7.5; 150 mM NaCl; 10 mM MgCl<sub>2</sub>; 1 mM DTT; 20 mM imidazole) and stored at  $\sim$ 80 °C. For lysis, cells were resuspended in  $\sim$ 30 ml lysis buffer with a tablet of Pierce EDTA-free protease inhibitor. Cells were lysed using a sonicator to deliver  $\sim$ 8,000 J of energy, and lysate was clarified at 18,000 r.p.m. in a JA-20 rotor (Beckman) for 30 min at 4 °C. Supernatant was applied to a 1 ml HisTrap column recirculating for  $\sim$ 30 min. The bound lysate was fractionated in a fast protein liquid chromatography system with five column volumes of lysis buffer and 10 column volumes of linear elution gradient from lysis buffer to lysis buffer, with 500 mM imidazole. Then 0.5 ml fractions were collected and analysed using SDS-polyacrylamide gel electrophoresis (SDS-PAGE). Fractions containing CCA-adding enzyme were combined and concentrated in a 30,000 Da molecular weight cut-off spin filter and buffer exchanged into buffer containing 20 mM HEPES, pH 7.5; 20 mM KCl; 1 mM EDTA; and 2 mM  $\beta$ -mercaptoethanol (BME). Protein was applied to a 1 ml heparin column and processed on a fast protein liquid chromatography system, as previously described<sup>52</sup>. Protein-containing fractions were

combined and dialysed against 20 mM HEPES, 150 mM NaCl, 10 mM MgCl<sub>2</sub>, 1 mM DTT and 20% glycerol, and stored at  $\sim$ 80 °C. The final concentration was 54  $\mu$ M in  $\sim$ 1 ml (extinction coefficient estimated at 55,350 M<sup>-1</sup> cm<sup>-1</sup>).

**3'NH<sub>2</sub>-ATP-tailing of N-1 tRNAs.** The procedure used for tRNA amino-tailing was adapted from ref. 53. Equimolar amounts of N-1 tRNA and *A. fulgidus* CCA-adding enzyme (usually 2  $\mu$ M) were combined in a reaction containing 100 mM glycine, pH 9; 10 mM MgCl<sub>2</sub>; 1 mM DTT; 0.002 U  $\mu$ l<sup>-1</sup> PPase; and 0.5 mM 2'-NH<sub>2</sub>-ATP (2'-amino-2'-deoxyadenosine-5'-triphosphate, purchased from Axxora). Reactions were incubated at 37 °C for 2 h. Degradation of tRNAs was seen if reactions were incubated past completion. NH<sub>2</sub>-tRNAs were extracted with 1:10 volume of 3 M NaOAc, pH 5.2, and one volume of acidic phenol chloroform; cleaned twice with one volume of chloroform; and precipitated with three volumes of EtOH. NH<sub>2</sub>-tRNAs were resuspended in water, and the reaction yield was analysed on a 10% acrylamide 7 M TBE urea gel (20 cm). Some 1–2 pmol of tRNA was loaded per lane, and the gel was stained with SYBR Green II after running. NH<sub>2</sub>-tRNAs were stored in aliquots at  $\sim$ 80 °C.

**Purification of MetRS.** The 6xHis-tagged MetRS expression plasmid was a gift from P. Ginther (Schepartz lab, University of California, Berkeley). The plasmid was transformed into BL21 (DE3) Codon+ RIL cells (T7 promoter). Culture overnights were diluted into ZYM-5052 autoinducing media<sup>54</sup> and expressed overnight at 37 °C. Cells were pelleted and resuspended in lysis buffer (20 mM Tris, pH 7.8; 150 mM NaCl; 5 mM imidazole; 0.5 mM EDTA;  $\sim$ 35 ml). Cells were lysed with a sonicator on ice until  $\sim$ 8,000 J had been delivered to the sample. Lysate was clarified by centrifugation at 18,000 r.p.m. (JA-20 rotor; Beckman) at 4 °C for 30 min. Supernatant was applied to a 5 ml HisTrap column, and the column was attached to a fast protein liquid chromatography system. Protein was purified on the fast protein liquid chromatography system by washing with five column volumes of lysis buffer with 23 mM imidazole and eluting with a linear gradient of 20 column volumes from 23–500 mM imidazole. Fractions containing the desired protein were pooled; dialysed overnight against 50 mM HEPES, pH 7.5, plus 100 mM KCl, 10 mM MgCl<sub>2</sub>, 7 mM BME and 30% glycerol; and then concentrated in spin filters. Protein was stored at  $\sim$ 80 °C in aliquots.

**Aminoacylation of tRNAs.** All aminoacylation reactions were performed in a buffer containing 50 mM HEPES, pH 7.5; 20 mM MgCl<sub>2</sub>; 10 mM KCl; 2 mM DTT; 10 mM ATP; 1:40 volume RNase inhibitor (murine, NEB); and 5–10 mM amino acid. Aminoacylation enzymes were usually used at 1  $\mu$ M, and tRNAs, at 2–5  $\mu$ M depending on stock concentration. Generally, a 1:5 enzyme/tRNA ratio was not exceeded. Reactions were incubated at 37 °C for 30 min and then extracted and precipitated as described in the previous section '3'NH<sub>2</sub>-ATP-tailing of N-1 tRNAs'.

### 70S ribosome preparation: Met–Met ribosome complex formation

All steps towards the Met–Met ribosome structure were performed essentially as described<sup>30</sup>. Briefly, the complex was formed by incubating 100 nM 70S ribosomes, 5  $\mu$ M mRNA,  $\sim$ 1.6  $\mu$ M Met-NH-tRNA<sup>fMet</sup> and 100  $\mu$ M paromomycin in buffer AC (20 mM Tris, pH 7.5; 100 mM NH<sub>4</sub>Cl; 15 MgCl<sub>2</sub>; 0.5 mM EDTA; 2 mM DTT; 2 mM spermidine; 0.05 mM spermine) for 30 min at 37 °C. The mRNA sequence GUUAAG**GAG**GUAAAUAUGAUGUAACUA was synthesized by Integrated DNA Technologies (Shine–Dalgarno sequence in bold;  $\times 2$  AUG codons underlined).

### Cryo-EM sample preparation

The sample was prepared for imaging on 300 mesh R1.2/1.3 UltrAuFoil grids with an additional layer of float-transferred amorphous carbon

support film. The grids were washed in chloroform prior to carbon floating. Before applying the sample, grids were glow discharged in a PELCO easiGlow at 0.39 mbar and 25 mA for 12 seconds. Some 4  $\mu$ l of sample was deposited onto each grid and left for 1 minute. The grid was then washed with a buffer containing 20 mM Tris, pH 7.5; 20 mM NH<sub>4</sub>Cl; 15 MgCl<sub>2</sub>; 0.5 mM EDTA; 2 mM DTT; 2 mM spermidine; and 0.05 mM spermidine by successively touching it to three 100  $\mu$ l drops of the buffer immediately prior to freezing. Grids were blotted and plunge-frozen in liquid ethane with an FEI Mark IV Vitrobot using the following settings: 4 °C, 100% humidity, blot force 6 and blot time 3. Grids were clipped for autoloading and stored in liquid N<sub>2</sub>.

### Cryo-EM data collection

Cryo-EM data collection parameters are summarized in Supplementary Table 2. Dose-fractionated videos were collected on a Titan Krios G3i microscope at an accelerating voltage of 300 kV and with a BioQuantum energy filter. Videos were recorded on a GATAN K3 direct electron detector operated in CDS mode. A total dose of 40 e<sup>-</sup> Å<sup>-2</sup> (e<sup>-</sup>, electron) was split over 40 frames per video. The magnification was 102,519 for a physical pixel size of 0.8296 Å and super-resolution pixel size of 0.4148 Å (based on a pixel size calibration performed after the final structure was obtained). Data collection was automated with SerialEM (ref. 55) v.3.8.2, which was also used for astigmatism correction by CTF and coma-free alignment by CTF. One video per hole was collected using stage shift to move between the centre holes of a 3 × 3 hole template and image shift to collect on the surrounding eight holes. The defocus ramp was set to range between -0.5 and -2  $\mu$ m.

### Image processing

RELION steps were performed in RELION v.3.1 and the beta of v4.0 (refs. 56,57). Motion correction was performed with MotionCor2 (ref. 58) v.1.0.1 within the RELION graphical user interface, and micrographs were binned to the physical pixel size (believed to be 0.81 Å at the outset). Contrast transfer function (CTF) parameters were estimated using CTFFind4 (ref. 59) v.4.1.5. Micrographs with poorly fitting CTF estimates were rejected based on visual inspection, leaving 6,673 videos for processing. Particle auto-picking was performed using the Laplacian-of-Gaussian method in RELION, yielding 1,021,926 particles. These were then extracted from the micrographs with rescaling to 1/8 the full size and underwent three rounds of two-dimensional (2D) classification. The 735,114 particles from the good 2D classes were then re-extracted at 1/4 the full size and imported into cryoSPARC (ref. 60) v.3.1.0 for heterogeneous refinement with six volume classes. The reference ribosome volume for this job was generated from PDB 1IVY coordinates<sup>24</sup> in EMAN2 (ref. 61). Two of the resulting classes corresponded to clean 70S volumes, so these classes were exported back to RELION and pooled (513,480 particles).

To separate out classes with different positions/rotation of the small subunit relative to the large subunit, 50S-focused refinement was first performed on all the particles, followed by 3D classification without alignment into five volume classes. In addition to subtle shifts in the 30S subunit, this step is useful for the removal of particles in minor states like those containing E-site tRNAs only, for example. From there, further pooling and focused classification on A-site and E-site tRNAs (without alignment) were performed, the details of which are summarized in Supplementary Fig. 1a. As all particles that were accepted at this stage contained P-site tRNAs, and the A and E sites appeared to produce more meaningful separation, classification on the P site was not pursued.

For the final structure, all particles in the three classes selected at the 30S rotation stage were extracted at full size and pooled for 50S-focused refinements prior to and in between CTF refinement<sup>62</sup>, Bayesian polishing<sup>63</sup> and CTF refinement again. This was to take advantage of the high resolution from the well-ordered large subunit and maximize particle number for optimum performance of these

jobs, and the resulting post-processed volume was also used for pixel size calibration. Particle classes of interest that had been identified earlier were separated again for final 50S-focused refinements using Python scripting to pull the appropriate subsets from the polished particle metadata.

From the classification procedure, there were three initial A-site classes that were examined individually as well as merged, and with and without further sorting on the E site. Ultimately, variation across maps indicated some residual disorder in fine details of the substrates, with some features alternately improved or worsened in different maps, and there was no single map representing the best set of features across A-site and P-site Met residues or their surroundings (Supplementary Fig. 1b). Taken together, it is clear that we are still somewhat limited by the inherent dynamics of substrates in the active site. Additionally, the line between meaningfully distinctive classes or conformations and the continuous motions of the complex(es) presents a challenge, particularly when particle number starts to become limiting. A merged map of two of the A-site classes was ultimately chosen for modelling, containing 129,455 particles and with a global resolution of the large subunit and tRNAs going to 2.1 Å resolution. A 30S-focused refinement was also performed for modelling purposes, which went to 2.3 Å resolution.

### Pixel size calibration

The pixel size was calibrated in Chimera (ref. 64) v.1.16 using the 'Fit to Map' function and the high-resolution pooled-particle map against the 50S subunit coordinates from the X-ray crystal structure of PDB 4YBB (ref. 65). The best cross-correlation value was obtained at a pixel size of 0.8296 Å. Half-maps for our refined volume were rescaled to the calibrated pixel size in Chimera, and post-processing was performed with these half-maps in RELION to obtain the Fourier shell correlation curve and final resolution estimate (Extended Data Fig. 2).

### Modelling

PDB 7K00 (ref. 30) was taken as a starting model. This model contained tRNA<sup>fMet</sup> in the P site and tRNA<sup>Val</sup> in the A site, whereas only tRNA<sup>fMet</sup> was used in the current work, so the A-site tRNA was replaced. Real-space refinement of the coordinates was performed in PHENIX (ref. 66; version dev-3051 and v.1.20.1-4487) into the 50S- and 30S-focused maps, and further adjustments to the model were done manually in Coot (ref. 67; v.0.9.4 and v.0.9.8.5), mainly around the PTC. Further additions to the model included Mg<sup>2+</sup> and K<sup>+</sup> ions, water molecules and spermidine ligands near the tRNA CCA ends, as well as residues 2–7 of r-protein bL27. The linkage between A-site and P-site tRNAs and Met monomers was modelled as an amide linkage to reflect experimental conditions for structure determination. As the 30S subunit was mainly included for model completeness, while the results are largely concerned with the 50S subunit, a map-versus-model Fourier shell correlation was calculated in PHENIX (ref. 66) for the 50S coordinates and focused map (Extended Data Fig. 2b). Model refinement statistics for the two subunits are summarized in Supplementary Table 2.

### Composite map

A composite cryo-EM map was calculated from the 2.1 Å 50S map and 2.3 Å 30S map for deposition. The 30S map was aligned to best fit the 30S region of the 50S map and resampled in Chimera. The two maps were set to have volume standard deviation values such that the small subunit (SSU) and large subunit (LSU) are visually balanced in the combined map. Coordinates for the 70S complex are fit to this composite map.

### Molecular dynamics simulations

As described in the Results, the starting point for our MD simulations was the RRM, which involved rigid-body docking of ordered Mg<sup>2+</sup> ions from PDB 7K00 into preliminary coordinates for the cryo-EM structure reported here, which ultimately included additional ions

not present in **7K00**. Static structures fail to capture the dynamic interactions between the RNA and ions<sup>68</sup>. Moreover, monovalent cations generally interact with RNA as highly dynamic species, creating a diffusive ion environment, while divalent cations, such as Mg<sup>2+</sup>, form an ion-hydration shell<sup>28,69,70</sup>. Hence, the rigid-body docking of the Mg<sup>2+</sup> ions from **7K00** described above was considered sufficient for our unbiased and biased MD calculations.

The resulting structure was solvated using the simple point charge water model<sup>71</sup>. K<sup>+</sup> and Cl<sup>-</sup> ions corresponding to 0.15 M concentration were added as well as K<sup>+</sup> counterions to neutralize the system. The final simulation box measured 95 Å along each side and consisted of ~88,000 atoms. The OPLS4 force field<sup>72</sup> and Desmond MD system (Schrödinger Release 2022-2) as implemented within Schrödinger Suite (release 2022-2) were used in this study. For fMet and all the non-L- $\alpha$ -amino acid monomers, the Force Field Builder (Schrödinger release 2022-2)<sup>72</sup> was used to parametrize the missing torsions, which it does by fitting the molecular mechanics torsional profiles to those obtained based on quantum mechanics calculations.

The systems were initially minimized and equilibrated with restraints on all solute heavy atoms, followed by production runs with all but the outer 10 Å C1' and C $\alpha$  atoms unrestrained. The constant-temperature, constant-pressure (NPT; number of particles  $N$ , pressure  $P$ , temperature  $T$ ) ensemble was used with constant temperature at 300 K and Langevin dynamics. The production runs were carried out for 300 ns in triplicate, changing the initial velocity seeds for each run. The conformational analysis, including the distances and angles, was calculated using Schrödinger's Python API (Schrödinger release 2022-2). The representative pose for the test fMet–Met run (Fig. 2c) was generated using the trajectory r.m.s.d.-based clustering method<sup>73</sup> as implemented in Maestro. The radial distribution function was generated using Schrödinger's built-in radial distribution function panel.

## Metadynamics

Desmond<sup>74</sup> (Schrödinger release 2022-2) was used for the metadynamics runs. The equilibration stage was the same as for the MD runs above, and the metadynamics production runs were carried out in duplicate (starting from different conformations as outlined above) for 100 ns each. The N $\alpha$ –C<sub>sp2</sub> distance and the Bürgi–Dunitz angle were used as collective variables. The biasing Gaussian potential ('hill') of 0.01 kcal mol<sup>-1</sup> was used, and a width of 0.15 Å for the N $\alpha$ –C<sub>sp2</sub> distance and 2.5° for the Bürgi–Dunitz angle  $\alpha_{BD}$  were applied. Analysis of the runs was performed with Schrödinger's Python API (Schrödinger release 2022-2) as well as in-house Python scripts.

## Reporting summary

Further information on research design is available in the Nature Portfolio Reporting Summary linked to this article.

## Data availability

The cryo-EM map and model reported here are deposited at the EM Data Bank and RCSB Protein Data Bank with accession codes [EMD-28257](#) for the 50S-focused map, [EMD-28256](#) for the 30S-focused map, [EMD-28255](#) for the 70S map, [EMD-28254](#) for the composite map and PDB [8EMM](#) for the full 70S complex coordinates aligned to the composite map. The coordinates of the RRM models representing metadynamics global minima are available at Zenodo: <https://doi.org/10.5281/zenodo.7730661>. The full MD and metadynamics trajectories are too large to upload at Zenodo (>50 GB); however, they are available upon reasonable request. Source data are provided with this paper.

## Code availability

Python scripts written using Schrödinger's API for the analysis of the data from the MD and metadynamics simulations, the metadynamics raw data for the free energy and the collective variables at each time

point, and the FES data are available at Zenodo: <https://doi.org/10.5281/zenodo.7714401>.

## References

- Kao, C., Zheng, M. & Rüdissler, S. A simple and efficient method to reduce nontemplated nucleotide addition at the 3' terminus of RNAs transcribed by T7 RNA polymerase. *RNA* **5**, 1268–1272 (1999).
- Ward, F. R., Watson, Z. L., Ad, O., Schepartz, A. & Cate, J. H. D. Defects in the assembly of ribosomes selected for  $\beta$ -amino acid incorporation. *Biochemistry* **58**, 4494–4504 (2019).
- Katoh, T. & Suga, H. Flexizyme-catalyzed synthesis of 3'-aminoacyl-NH-tRNAs. *Nucleic Acids Res.* **47**, e54 (2019).
- Studier, F. W. Stable expression clones and auto-induction for protein production in *E. coli*. *Methods Mol. Biol.* **1091**, 17–32 (2014).
- Mastronarde, D. N. Automated electron microscope tomography using robust prediction of specimen movements. *J. Struct. Biol.* **152**, 36–51 (2005).
- Zivanov, J. et al. New tools for automated high-resolution cryo-EM structure determination in RELION-3. *eLife* **7**, e42166 (2018).
- Kimanius, D., Dong, L., Sharov, G., Nakane, T. & Scheres, S. H. W. (2021) New tools for automated cryo-EM single-particle analysis in RELION-4.0. *Biochem. J.* **478**, 4169–4185 (2021).
- Zheng, S. Q. et al. MotionCor2: anisotropic correction of beam-induced motion for improved cryo-electron microscopy. *Nat. Methods* **14**, 331–332 (2017).
- Rohou, A. & Grigorieff, N. CTFFIND4: fast and accurate defocus estimation from electron micrographs. *J. Struct. Biol.* **192**, 216–221 (2015).
- Punjani, A., Rubinstein, J. L., Fleet, D. J. & Brubaker, M. A. cryoSPARC: algorithms for rapid unsupervised cryo-EM structure determination. *Nat. Methods* **14**, 290–296 (2017).
- Tang, G. et al. EMAN2: an extensible image processing suite for electron microscopy. *J. Struct. Biol.* **157**, 38–46 (2007).
- Zivanov, J., Nakane, T. & Scheres, S. H. W. Estimation of high-order aberrations and anisotropic magnification from cryo-EM data sets in RELION-3.1. *IUCrJ* **7**, 253–267 (2020).
- Zivanov, J., Nakane, T. & Scheres, S. H. W. A Bayesian approach to beam-induced motion correction in cryo-EM single-particle analysis. *IUCrJ* **6**, 5–17 (2019).
- Pettersen, E. F. et al. UCSF Chimera—a visualization system for exploratory research and analysis. *J. Comput. Chem.* **25**, 1605–1612 (2004).
- Noeske, J. et al. High-resolution structure of the *Escherichia coli* ribosome. *Nat. Struct. Mol. Biol.* **22**, 336–341 (2015).
- Liebschner, D. et al. Macromolecular structure determination using X-rays, neutrons and electrons: recent developments in Phenix. *Acta Crystallogr. D Struct. Biol.* **75**, 861–877 (2019).
- Emsley, P., Lohkamp, B., Scott, W. G. & Cowtan, K. Features and development of Coot. *Acta Crystallogr. D Struct. Biol.* **66**, 486–501 (2010).
- Lipfert, J., Doniach, S., Das, R. & Herschlag, D. Understanding nucleic acid–ion interactions. *Annu. Rev. Biochem.* **83**, 813–841 (2014).
- Rangan, P. & Woodson, S. A. Structural requirement for Mg<sup>2+</sup> binding in the group I intron core. *J. Mol. Biol.* **329**, 229–238 (2003).
- Sun, L.-Z., Zhang, D. & Chen, S.-J. Theory and modeling of RNA structure and interactions with metal ions and small molecules. *Annu. Rev. Biophys.* **46**, 227–246 (2017).
- Berendsen, H. J. C., Postma, J. P. M., van Gunsteren, W. F. & Hermans, J. in *Intermolecular Forces: Proceedings of the Fourteenth Jerusalem Symposium on Quantum Chemistry and Biochemistry Held in Jerusalem, Israel, April 13–16, 1981* (ed. Pullman, B.) 331–342 (Springer Netherlands, 1981).

72. Lu, C. et al. OPLS4: improving force field accuracy on challenging regimes of chemical space. *J. Chem. Theory Comput.* **17**, 4291–4300 (2021).
73. Frey, B. J. & Dueck, D. Clustering by passing messages between data points. *Science* **315**, 972–976 (2007).
74. Phillips, J. C. et al. Scalable molecular dynamics on CPU and GPU architectures with NAMD. *J. Chem. Phys.* **153**, 044130 (2020).

## Acknowledgements

This work was supported by the National Science Foundation Center for Genetically Encoded Materials (C-GEM), CHE 2002182. We are grateful to S. Smaga and J. Walker for insights regarding monomer selection, to D. Lupyan and C. de Oliveira (Schrödinger) for insights regarding MD and metadynamics simulations and to M. Repasky (Schrödinger) and members of the Cate and Schepartz labs for comments on the manuscript. We also thank the Cal-Cryo facility, D. Toso and P. Tobias for assistance with cryo-EM data acquisition and management.

## Author contributions

S.J.M., J.H.D.C., A.S. and A.M.A. conceived the study. A.M.A., Z.L.W., I.J.K., J.H.D.C., S.J.M. and A.S. designed the project. A.M.A. led the computational experiments and analysis. Z.L.W. led the cryo-EM experiments and analysis. F.R.W. prepared ribosomal complexes for

cryo-EM. A.M.A., Z.L.W., I.J.K., J.H.D.C., S.J.M. and A.S. analysed and interpreted the data. Z.L.W., I.J.K., S.J.M., J.H.D.C., A.S. and A.M.A. prepared the manuscript.

## Competing interests

The authors declare no competing interests.

## Additional information

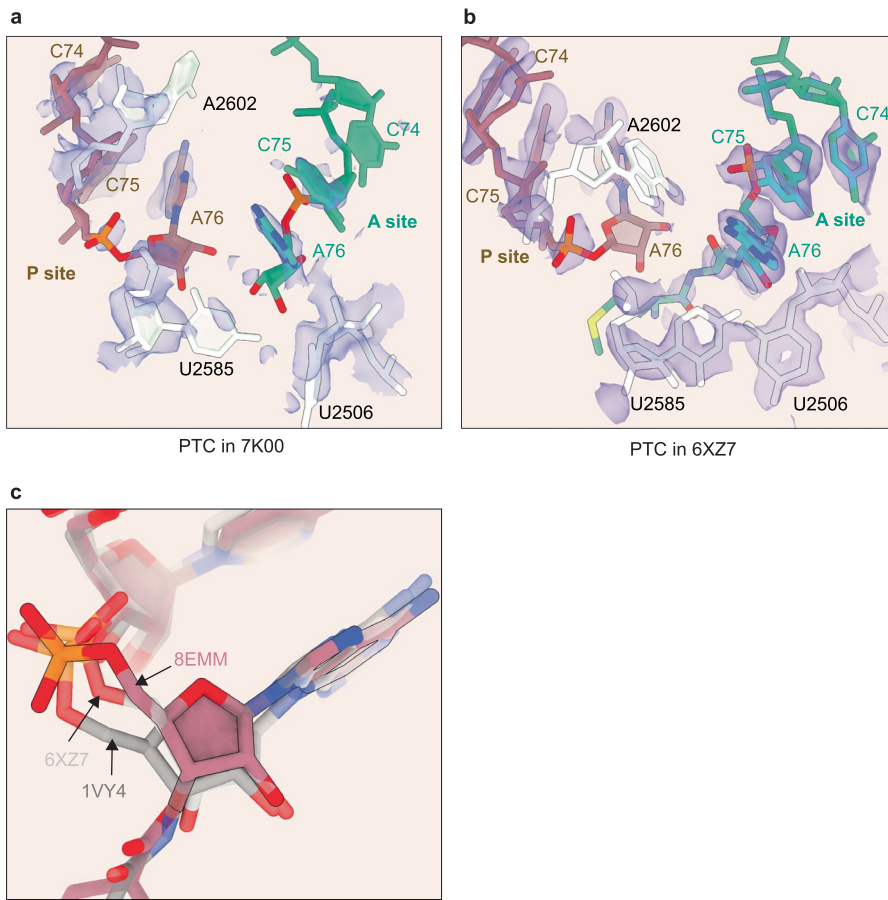
**Extended data** is available for this paper at <https://doi.org/10.1038/s41557-023-01226-w>.

**Supplementary information** The online version contains supplementary material available at <https://doi.org/10.1038/s41557-023-01226-w>.

**Correspondence and requests for materials** should be addressed to Scott J. Miller, Jamie H. D. Cate, Alanna Schepartz or Ara M. Abramyan.

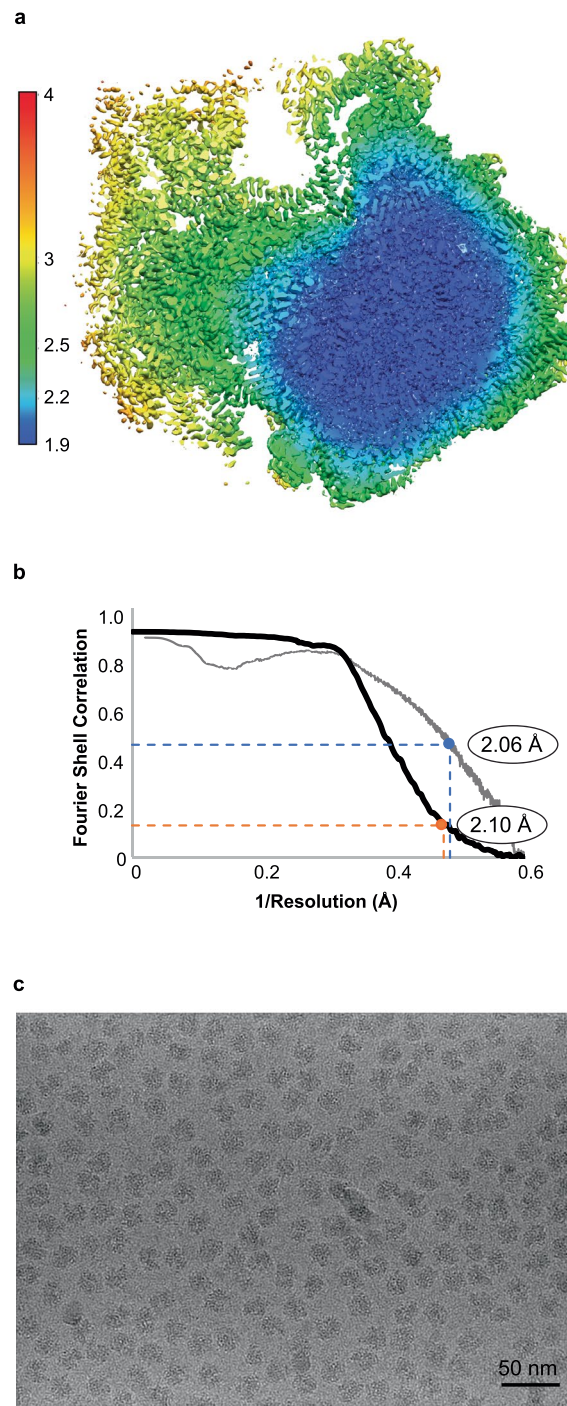
**Peer review information** *Nature Chemistry* thanks Giulia Palermo and the other, anonymous, reviewer(s) for their contribution to the peer review of this work.

**Reprints and permissions information** is available at [www.nature.com/reprints](http://www.nature.com/reprints).



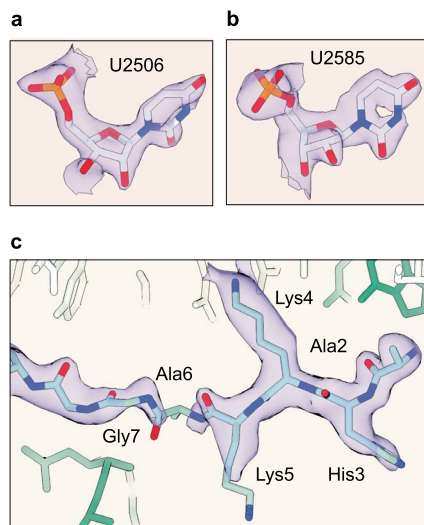
**Extended Data Fig. 1 | Details in the PTC of prior structures.** **a**, Close-up of the PTC in PDB 7K00 illustrates the poor quality of local density in this map (indigo) around the P site (rose) and A site (green) tRNAs. PTC bases U2506, U2585, and A2602 of the 23S rRNA are shown in white. The deposited 50S-focused map is shown with an additional B-factor of  $30 \text{ \AA}^2$  applied, supersampled for smoothness. **b**, Close-up of the PTC in PDB 6XZ7, showing dipeptide in the A site (green with atomistic coloring) and uncharged P-site tRNA (rose). The map has been supersampled for smoothness. Contour levels for maps shown in

both **a** and **b** are chosen to illustrate disorder relative to better-resolved map regions, but lower contour levels and/or higher B-factor blurring brings out features supporting models. Labels for A- and P-site tRNAs in **a** and **b** are color-matched to the carbon atoms, and 23S rRNA bases are labeled in black. **c**, P-site tRNA A76 backbone conformation in our model (pink, black outline) compared to 6XZ7 (light gray) and 1VY4 (dark gray). Labels indicating the models are color-matched to the carbon atoms.

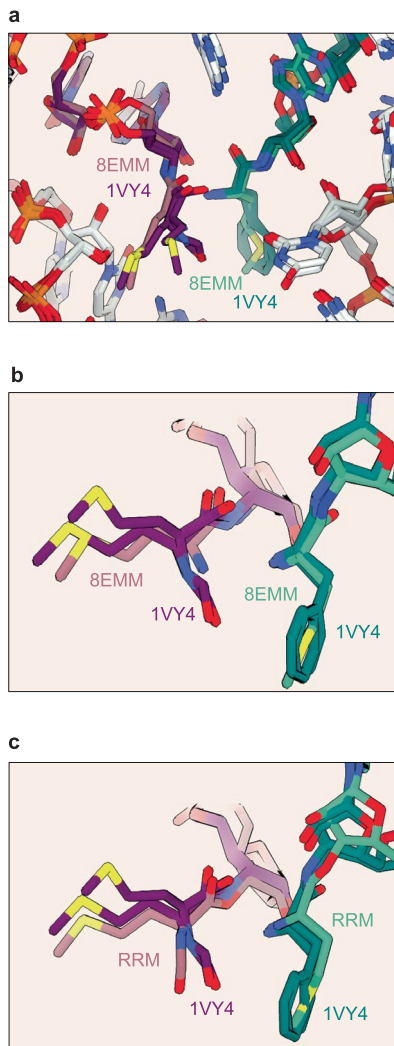


**Extended Data Fig. 2 | Resolution of the 50S subunit in the Met-Met ribosome structure.** **a**, Local resolution of the 50S-focused cryo-EM map; **b**, FSC curves indicating resolution of the 50S subunit. Half-map FSC (black) is at 2.10 Å at the gold-standard cutoff value 0.143; map-vs.-model FSC (gray) is at 2.06 Å at

the 0.5 cutoff. Only the large subunit was masked for the half-map FSC, and **c**, representative micrograph showing individual ribosome particles. The micrograph was low-pass filtered to 20 Å for easier visualization of particles.

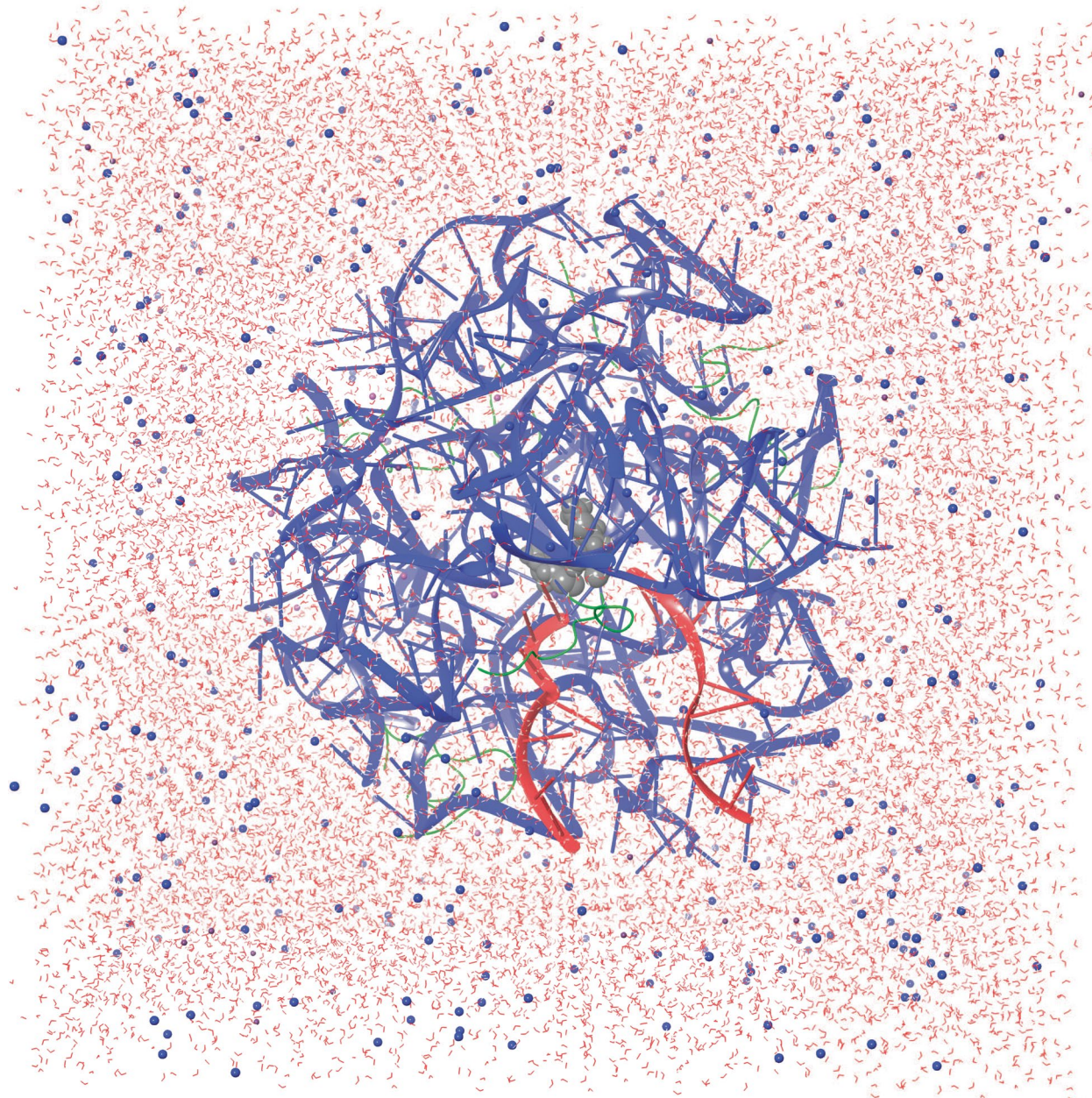


**Extended Data Fig. 3 | Structural model of U2506, U2585, and the N-terminus of ribosomal protein bL27.** **a, b**, bases U2506 and U2585 of the 23S rRNA modelled in the cryo-EM density. The map here has been post-processed with a B-factor of  $-13 \text{ \AA}^2$  and supersampled for smoothness. **c**, Newly modelled section of r-protein bL27 (Ala-2 to Gly-7) (light blue). 23S rRNA is shown in white and A-site tRNA in green, with EM density shown in indigo. The map here has been post-processed with a B-factor of  $10 \text{ \AA}^2$ .



**Extended Data Fig. 4 | Orientation of the P-site monomer in the PTC is affected minimally by the presence or absence of a N-terminal formyl group.** **a**, Superposition and **b**, close-up view of the PTC regions of 1VY4 (purple and teal) with that of 8EMM, the cryo-EM model reported here (rose and green). 23S rRNA is shown in white. Two structures are shown for 1VY4 because there are two ribosome structures in the unit cell. **c**, Superposition of the PTC regions of 1VY4 with the lowest energy pose of the metadynamics simulation of the RRM (in which the P-site tRNA has been altered in silico to carry fMet). The identity of

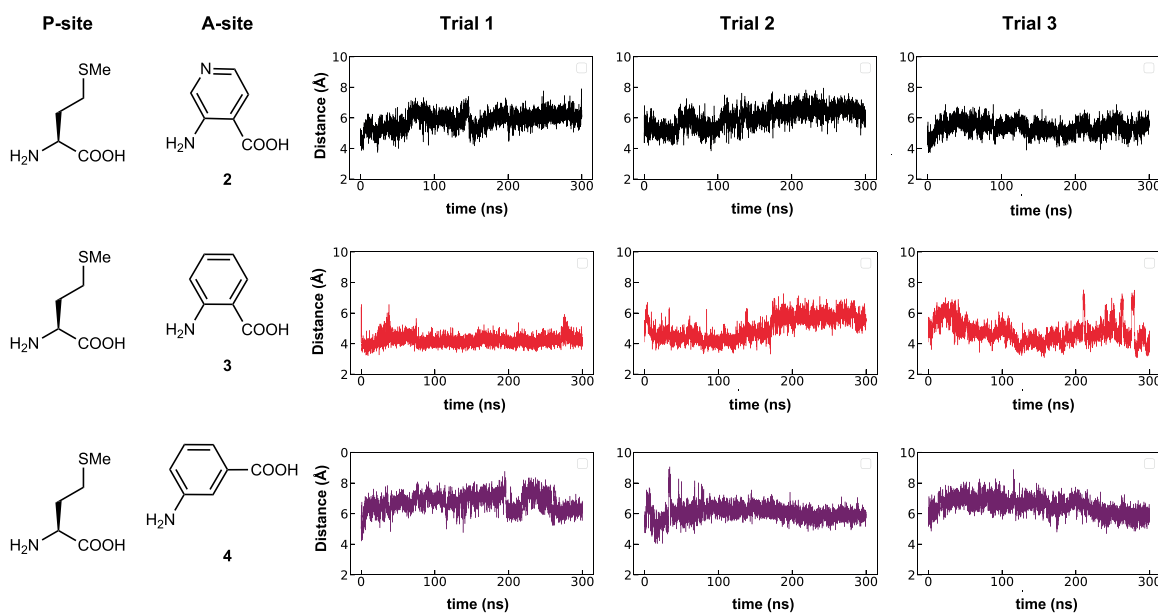
the models 8EMM, 1VY4, and the RRM are indicated for both A and P sites with model-matched colors. These images reveal excellent superposition of the carbonyl groups (red) that are attacked during amide bond formation and the three P-site N atoms (in blue), regardless of whether that N is attached to protons alone or a formyl group. This analysis suggests that the presence or absence of a formyl group on the P-site tRNA has little or no effect on monomer placement within the PTC from the standpoint of structural biology.



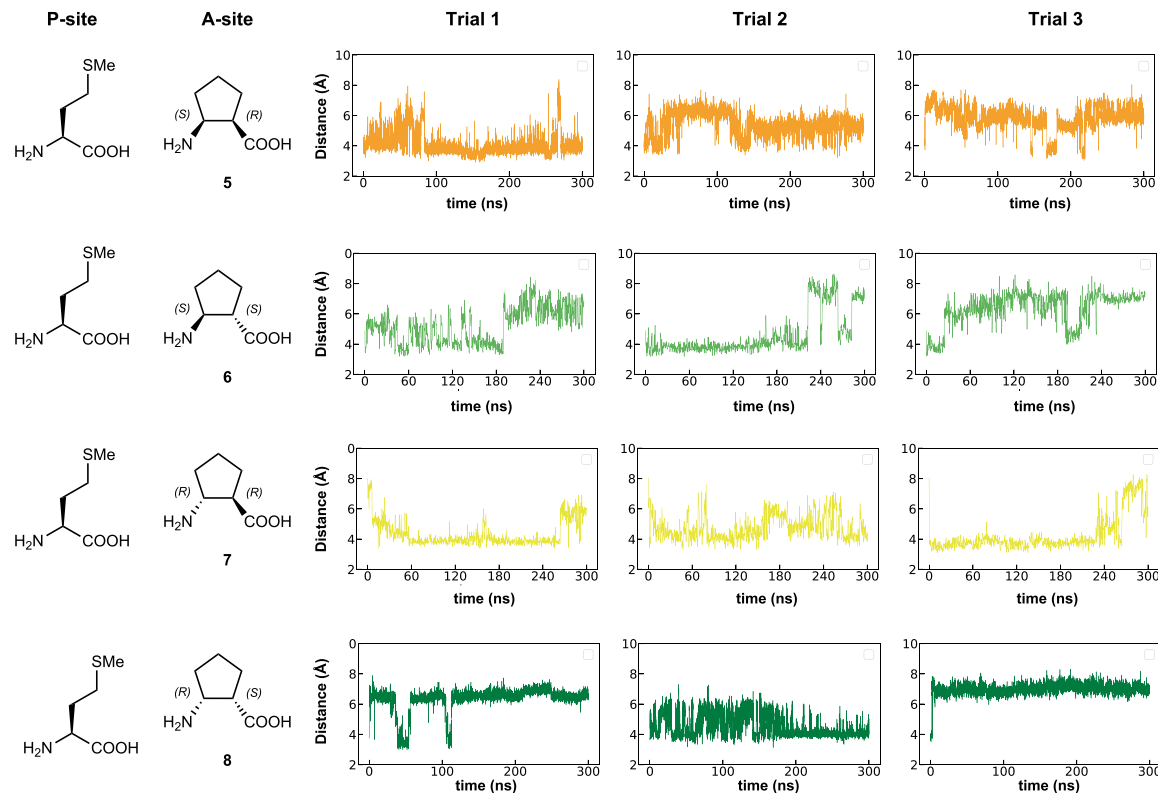
**Extended Data Fig. 5 | Image showing the simulation box used for molecular dynamics (MD) and metadynamics simulations.** The 30 Å Reduced Ribosomal Model (RRM) is shown in the center in cartoon representation, wherein the RNAs

of the 50S subunit are in blue, the protein residues are in green, the tRNAs are in red, and the monomers are in gray CPK representation. The water molecules are in red line representation, whereas the ions ( $\text{K}^+$ ,  $\text{Cl}^-$ ,  $\text{Mg}^{2+}$ ) are in blue spheres.

a

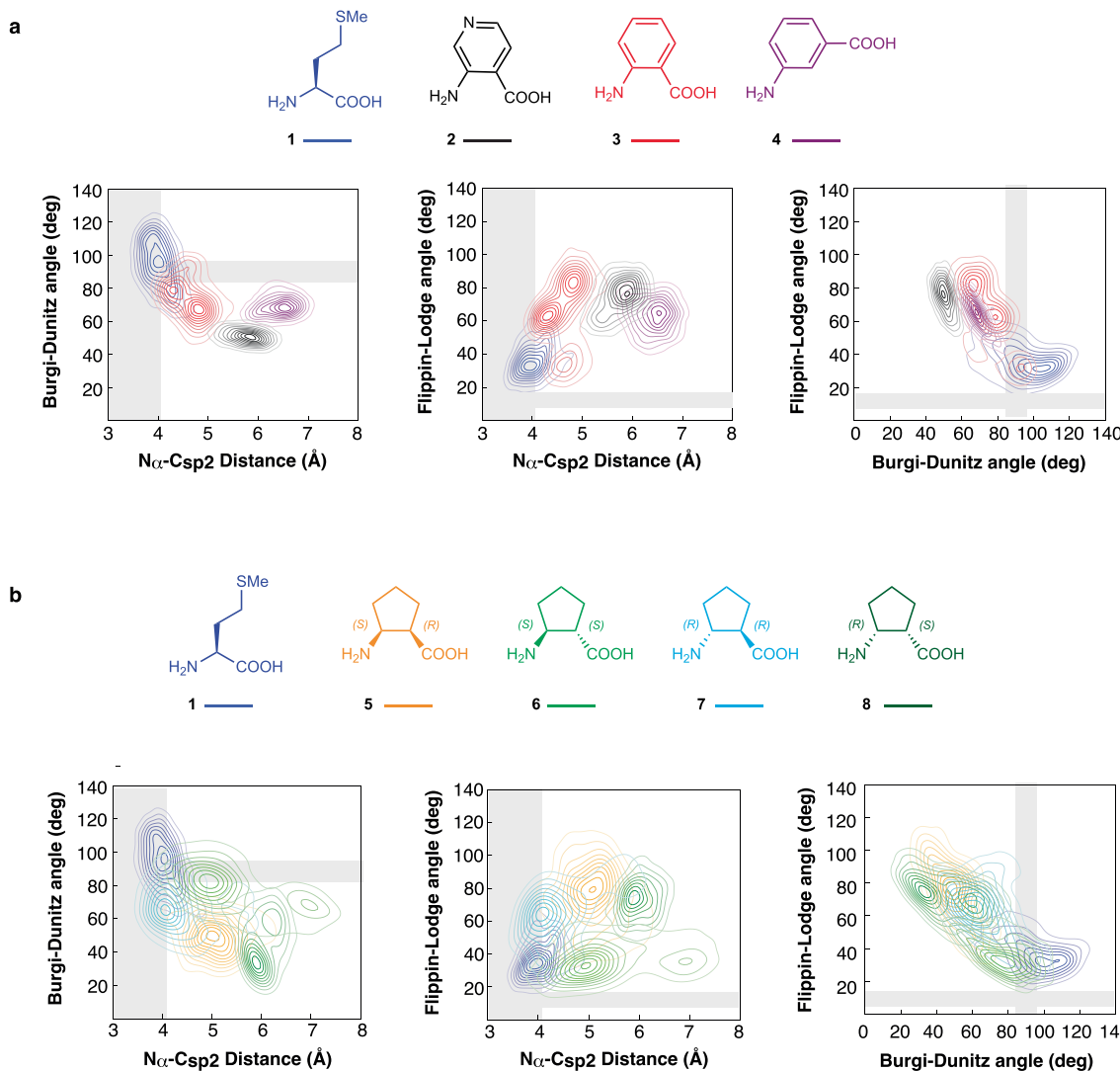


b



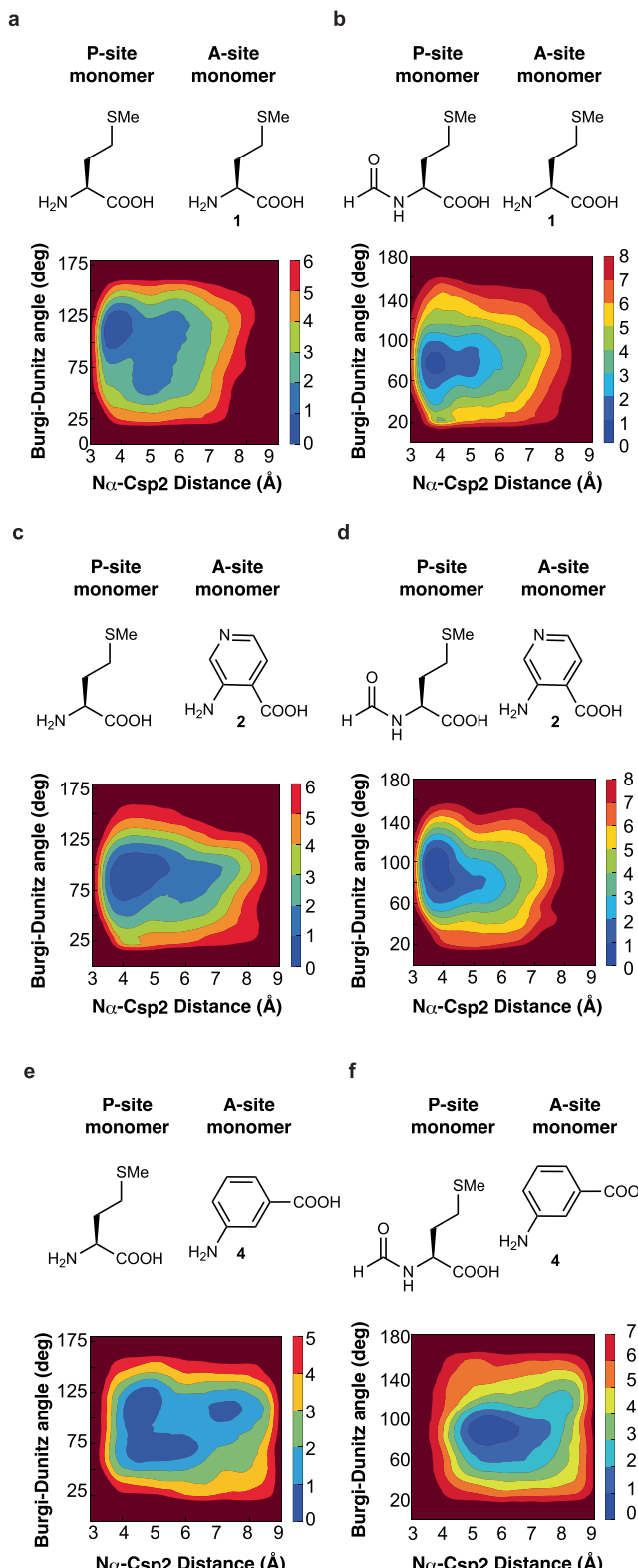
**Extended Data Fig. 6 | Trajectories from MD simulations of different monomers in the A site.** Trajectories illustrating evolution of the distance between the A-site nucleophile ( $\text{N}\alpha$ ) and the P-site fMet carbonyl electrophile ( $\text{Csp}2$ ) over 300 ns within the 30 Å Reduced Ribosome Model (RRM). **a**, amino-benzoic acids **2–4**; **b**,  $\beta^{2,3}$ -2-aminocyclopentane-1-carboxylic acids **5–8**. We used

Schrödinger's Force Field Builder (Schrödinger release 2022-1) to parametrize the existing OPLS4 force field to accurately describe the conformational dynamics of each new monomer. Maestro's 3D Builder was then used to assemble the new ester bond and minimize the system to release clashes with surrounding residues.



**Extended Data Fig. 7 | Scatter plots of the three geometric measurements used to evaluate conformational fluctuations.** **a**, fluctuations of aminobenzoic acids **2–4** and **b**, fluctuations of cyclic  $\beta^{2,3}$ -amino acid 2-aminocyclopentane-1-carboxylic acid monomers **5–8** in comparison to Met **1** in the PTC of the RRM throughout the MD runs are shown. Specifically, the  $\text{N}\alpha\text{-Csp2}$  distance is plotted

against either the Bürgi–Dunitz angle  $\alpha\text{BD}$  (left) or the Flippin–Lodge angle  $\alpha\text{FL}$  (center), and the two angles are plotted against each other (right). The gray zones highlight  $\text{N}\alpha\text{-Csp2}$  distances of between 3 and 4 Å, and values of  $\alpha\text{BD}$  and  $\alpha\text{FL}$  of between 90° and 105° and 5° to 20°, respectively.



**Extended Data Fig. 8 | Plots of free energy surfaces from metadynamics simulations: the effect of a P-site N-terminal formyl group.** Free energy surfaces (FES) (kcal/mol) of the 30 Å RRM model containing an P-site tRNA acylated with **a, c, e**, Met or **b, d, f**, fMet plotted along the Bürgi–Dunitz angle  $\alpha$ BD and  $N\alpha$ –Csp2 distance collective variables. A-site tRNAs were acylated with **a, b** Met **1**; **c, d**, aminobenzoic acid **2**; **e, f**, aminobenzoic acid **4**.

acylated with **a, c, e**, Met or **b, d, f**, fMet plotted along the Bürgi–Dunitz angle  $\alpha$ BD and  $N\alpha$ –Csp2 distance collective variables. A-site tRNAs were acylated with **a, b** Met **1**; **c, d**, aminobenzoic acid **2**; **e, f**, aminobenzoic acid **4**.

## Reporting Summary

Nature Portfolio wishes to improve the reproducibility of the work that we publish. This form provides structure for consistency and transparency in reporting. For further information on Nature Portfolio policies, see our [Editorial Policies](#) and the [Editorial Policy Checklist](#).

### Statistics

For all statistical analyses, confirm that the following items are present in the figure legend, table legend, main text, or Methods section.

n/a Confirmed

- The exact sample size ( $n$ ) for each experimental group/condition, given as a discrete number and unit of measurement
- A statement on whether measurements were taken from distinct samples or whether the same sample was measured repeatedly
- The statistical test(s) used AND whether they are one- or two-sided  
*Only common tests should be described solely by name; describe more complex techniques in the Methods section.*
- A description of all covariates tested
- A description of any assumptions or corrections, such as tests of normality and adjustment for multiple comparisons
- A full description of the statistical parameters including central tendency (e.g. means) or other basic estimates (e.g. regression coefficient) AND variation (e.g. standard deviation) or associated estimates of uncertainty (e.g. confidence intervals)
- For null hypothesis testing, the test statistic (e.g.  $F$ ,  $t$ ,  $r$ ) with confidence intervals, effect sizes, degrees of freedom and  $P$  value noted  
*Give  $P$  values as exact values whenever suitable.*
- For Bayesian analysis, information on the choice of priors and Markov chain Monte Carlo settings
- For hierarchical and complex designs, identification of the appropriate level for tests and full reporting of outcomes
- Estimates of effect sizes (e.g. Cohen's  $d$ , Pearson's  $r$ ), indicating how they were calculated

*Our web collection on [statistics for biologists](#) contains articles on many of the points above.*

### Software and code

Policy information about [availability of computer code](#)

Data collection SerialEM version 3.8.2

Data analysis RELION 3.1, cryoSPARC v3.1.0, MotionCor2 v1.0.1, CTFFind4 v4.1.5, PHENIX versions dev-3051 and 1.20.1-4487, Coot versions 0.9.4 and 0.9.8.5, Chimera v1.16, ChimeraX v1.3, Schrödinger Release 2022-2

For manuscripts utilizing custom algorithms or software that are central to the research but not yet described in published literature, software must be made available to editors and reviewers. We strongly encourage code deposition in a community repository (e.g. GitHub). See the Nature Portfolio [guidelines for submitting code & software](#) for further information.

### Data

Policy information about [availability of data](#)

All manuscripts must include a [data availability statement](#). This statement should provide the following information, where applicable:

- Accession codes, unique identifiers, or web links for publicly available datasets
- A description of any restrictions on data availability
- For clinical datasets or third party data, please ensure that the statement adheres to our [policy](#)

The cryo-EM map and model reported here are deposited at the EMDDataBank and RCSB Protein Databank with accession codes EMD-28257 for the 50S-focused map, EMD-28256 for the 30S-focused map, EMD-28255 for the 70S map, EMD-28254 for the composite map, and PDB 8EMM for the full 70S complex coordinates aligned to the composite map. The coordinates of the RRM models for MetaD global minima are available using this link: 30A\_RRMs.

## Human research participants

Policy information about [studies involving human research participants and Sex and Gender in Research](#).

Reporting on sex and gender

N/A

Population characteristics

N/A

Recruitment

N/A

Ethics oversight

N/A

Note that full information on the approval of the study protocol must also be provided in the manuscript.

## Field-specific reporting

Please select the one below that is the best fit for your research. If you are not sure, read the appropriate sections before making your selection.

Life sciences       Behavioural & social sciences       Ecological, evolutionary & environmental sciences

For a reference copy of the document with all sections, see [nature.com/documents/nr-reporting-summary-flat.pdf](https://nature.com/documents/nr-reporting-summary-flat.pdf)

## Life sciences study design

All studies must disclose on these points even when the disclosure is negative.

Sample size

N/A

Data exclusions

N/A

Replication

N/A

Randomization

N/A

Blinding

N/A

## Reporting for specific materials, systems and methods

We require information from authors about some types of materials, experimental systems and methods used in many studies. Here, indicate whether each material, system or method listed is relevant to your study. If you are not sure if a list item applies to your research, read the appropriate section before selecting a response.

### Materials & experimental systems

n/a	Involved in the study
<input checked="" type="checkbox"/>	<input type="checkbox"/> Antibodies
<input checked="" type="checkbox"/>	<input type="checkbox"/> Eukaryotic cell lines
<input checked="" type="checkbox"/>	<input type="checkbox"/> Palaeontology and archaeology
<input checked="" type="checkbox"/>	<input type="checkbox"/> Animals and other organisms
<input checked="" type="checkbox"/>	<input type="checkbox"/> Clinical data
<input checked="" type="checkbox"/>	<input type="checkbox"/> Dual use research of concern

### Methods

n/a	Involved in the study
<input checked="" type="checkbox"/>	<input type="checkbox"/> ChIP-seq
<input checked="" type="checkbox"/>	<input type="checkbox"/> Flow cytometry
<input checked="" type="checkbox"/>	<input type="checkbox"/> MRI-based neuroimaging